

Gold Nanobipyramids Coated with Silver–Platinum Alloy Shells for Plasmonically Enhanced Photocatalytic Degradation of Methyl Orange

Er-Ji Zhang, Tian-Song Deng,* Yu-Chun Cheng, Li-Yong Liu, Jia-Fei Gao, Jiahong Wen, Xiaoyu Zhao, and Jie Liu



Cite This: *ACS Appl. Nano Mater.* 2024, 7, 14596–14608



Read Online

ACCESS |



Metrics & More



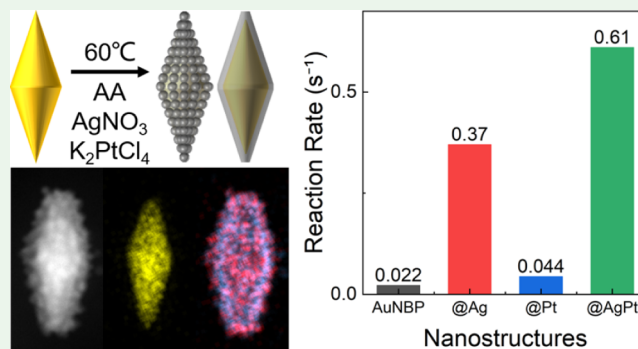
Article Recommendations



Supporting Information

ABSTRACT: Plasmonic multimetal materials, consisting of a plasmonic core and a catalytic shell in a core–shell structure, often exhibit excellent catalytic performances. Such excellent performances arise from the synergistic collaboration between the plasmonic core's localized surface plasmon-excited hot electrons and the catalytically active sites of the catalytic shell. In this context, a trimetallic nanostructure was designed featuring gold nanobipyramids (AuNBP) with a silver–platinum alloy shell, serving as a plasmon-mediated photocatalyst for the degradation of methyl orange (MO) under visible and near-infrared light. By altering the concentrations of the surfactants hexadecyltrimethylammonium bromide (CTAB) and hexadecyltrimethylammonium chloride (CTAC), the resulting nanostructure can take on either island-like or shell-like morphology. In the model system of the photocatalytic reaction of MO, employing the synthesized nanoparticles as catalysts, the study investigated the reaction under xenon lamp illumination. The trimetallic nanostructure exhibited robust photocatalytic performances, surpassing AuNBP by a factor of 27.8. The transfer of plasmon resonance energy from AuNBP to the silver–platinum alloy layer, augmenting the generation of charge carriers, elucidates its outstanding photocatalytic performance. The obtained trimetallic nanostructure showcases promising potential applications in the realm of photocatalysis, contributing to the development of advanced plasmon-enhanced photocatalysts with enhanced efficiency and multifunctionality.

KEYWORDS: gold nanobipyramids, trimetallic nanostructure, surface plasmon resonance, photocatalysis, nanoparticle



1. INTRODUCTION

Metal nanoparticles support localized surface plasmon resonances (LSPRs), also known as plasmonic nanoparticles. This phenomenon arises from the collective oscillations of conduction electrons confined to the nanoscale. Due to their unique optical properties, plasmonic metal nanoparticles find numerous applications in various fields, including nanooptics,¹ chemical and biological sensing,^{2,3} photocatalysis,⁴ biotechnology,⁵ and solar energy harvesting.⁶ To meet the diverse needs of different technological applications, various plasmonic nanoparticles have been synthesized. Among them, those composed of gold (Au) and silver (Ag) are the most commonly employed, owing to their outstanding ability to generate localized surface plasmons. Nanospheres and nanorods are perhaps the most popular nanostructures in the field of nanoplasmonics.

AuNBPs and gold nanorods (AuNRs) are two types of elongated plasmonic nanoparticles that can be synthesized and tuned in their longitudinal dipole plasmon wavelengths from the visible to the near-infrared range.⁷ Both of them exhibit

highly polarization-dependent absorption and scattering cross sections due to their geometric shapes.^{8,9} In terms of their distinctions, each AuNBP features twin planes with five angularly spaced facets parallel to the length direction, while the most common AuNRs are typically single crystalline.^{10–12} Consequently, AuNBPs have two sharp tips, whereas AuNRs have rounded or flattened ends, leading to significantly different plasmonic properties. In general, AuNBPs demonstrate larger local field enhancements, greater optical cross sections, narrower line widths, better shape and size consistency, and higher refractive index sensitivity compared to that of the AuNRs.¹³ With the recent emergence of reliable methods for growing high-purity and uniform AuNBPs,^{14–16}

Received: April 11, 2024

Revised: May 21, 2024

Accepted: May 31, 2024

Published: June 7, 2024



they have garnered widespread interest among researchers for studying their intriguing plasmonic properties and applications.^{17–23}

Plasmonic multimetal nanostructures have attracted significant interest due to their unique shapes and material-dependent catalytic, optical, electrical, and magnetic properties.^{24–31} They combine the plasmonic functionality of metal nanoparticles with the physical and chemical properties of other metals, such as catalytic activity, magnetism, optical imaging, and cancer treatment. Due to the LSPR field enhancement effect of plasmonic metal nanostructures, multimetal nanostructures with plasmonic properties have extensive application potential in areas such as photochemistry,³² optomagnetism,³³ optoelectronics,³⁴ and photobiology.³⁵ Among all applications of plasmonic multimetal nanostructures, one of the most in-depth and popular research topics is photocatalysis.^{36–38} It can be applied to special chemical reactions, such as pollutant degradation, water splitting, and organic synthesis. Excellent photocatalysts can meet the industrial demand for high reaction efficiency and cost-effectiveness. Khodabandloo et al.³⁹ discussed the use of semiconductor photocatalysis for the removal and mineralization of various pollutants. The review covers the preparation methods and mechanisms of various semiconductor catalysts, provides suggestions for improving semiconductor efficiency in photocatalysis, and discusses a range of pollutants including organic compounds, heavy metals, pharmaceutical pollutants, pesticides, and microorganisms. It also highlights the latest applications of semiconductors in photocatalytic remediation.

In general, the catalytic performance of multimetal nanostructure is provided by two main components. One part consists of common plasmonic nanoparticles, such as Au and Ag,^{40–42} while the other part consists of common catalysts, such as palladium (Pd) and platinum (Pt).^{43,44} Plasmonic nanoparticles can generate LSPR, which is caused by the coherent oscillation of conduction band electrons in the medium, leading to the production of intense local electric fields and hot electrons. More importantly, for known rod-shaped plasmonic nanostructures, their plasmonic characteristics, specifically the longitudinal plasmon resonance wavelength, can be adjusted across the entire visible and near-infrared spectrum. This adjustment depends on factors, such as the shape and size of the nanostructures. However, traditional plasmonic nanoparticle catalysts are suitable only for specific reactions, and common catalytic nanoparticles do not support strong LSPR in the visible and near-infrared regions. In past studies, bimetallic nanoparticles composed of plasmonic cores and catalytic shells have demonstrated excellent catalytic performance.^{45–51} For instance, Chen et al.⁵² modified platinum particles on the surface of AuNRs and used them as catalysts in the reduction reaction of nonfluorescent Rhodamine B to highly fluorescent triphenylmethane with N₂H₄. This catalyst exhibited strong catalytic performance under both illuminated and nonilluminated conditions. Yun et al.⁵³ reported a method for preparing Au nanoframe@Pd (Au NF@Pd) array electrocatalysts in the presence of cetylpyridinium chloride. Compared to both Au NF@Pd nanostructures and Au NBP@Pd arrays, the Au NF@Pd array demonstrated stronger electrocatalytic performance for ethanol electrooxidation due to its abundant catalytically active sites. Compared to commercial Pd/C electrocatalysts, the Au NF@Pd array exhibited 4.1 times higher specific activity and 13.7 times higher mass activity. Chen et al.⁵⁴ reported on two

configurations of AuNR@Pd nanostructures: one where the nanorod core was covered by a continuous palladium shell, and another where it was covered by discrete palladium nanoparticles. The study explored the plasmonic percolation behavior of these AuNR@Pd nanostructures. Single-particle scattering measurements and FDTD numerical simulations further confirmed the presence of plasmonic percolation. Gholipour et al.⁵⁵ described the preparation of single-layer carbon nitride-modified plasmonic AgPd alloy nanoparticles (AgPdNPs/SLCN) using an ultrasound-assisted hydrothermal method. These nanoparticles were used for photocatalytic hydrogen production from formic acid at a near-room temperature (30 °C). The catalytic activity of the palladium atoms was synergistically enhanced by the LSPR effect of the silver atoms, greatly improving the photocatalytic performance. Shokouhimehr et al.⁵⁶ reported the design of a magnetically recoverable core–shell palladium nanocatalyst for the efficient oxidation of alcohols under base-free aqueous conditions. The nanocatalyst exhibited high catalytic activity in other types of reactions involving Pd NPs, such as Suzuki cross-coupling and reduction of nitroarenes. It also demonstrated a certain degree of stability under harsh reaction conditions. Alamgholiloo et al.⁵⁷ described a novel and efficient strategy for anchoring Fe₃O₄ nanoparticles on graphene oxide (GO) sheet-supported metal–organic frameworks (MOFs). The prepared Fe₃O₄/Cu-BDC/GO nanocatalyst, characterized and studied using various methods, significantly enhanced the catalytic performance of alcohol oxidation reactions under very mild and sustainable reaction conditions, especially when used in conjunction with the cocatalyst 2,2,6,6-tetramethylpiperidine-N-oxide. Ahadi et al.⁵⁸ reported the synthesis of bridged dimeric organic functionalized viologen PMOs on titanium dioxide (TiO₂) via a layer-by-layer growth method. The prepared material successfully developed a novel mixed photo-oxidation system, which could be used for the mineralization of formic acid under sunlight irradiation.

However, Pt (or Pd) possesses a large imaginary part of the dielectric function, resulting in significant plasmonic damping. When the plasmonic nanoparticles are covered by a Pt (or Pd) shell, the intensity of LSPR significantly decreases and the width broadens because the LSPR of core–shell nanostructures primarily depends on the material in the shell. This substantial plasmonic damping leads to a poorer catalytic performance. For example, Yong et al.⁵⁹ investigated the catalytic performance of Au nanoparticles with different thicknesses of Pd shell coverage and found that thicker shells led to lower reaction rates. Therefore, designing a plasmon-mediated photocatalyst with a catalytic shell while retaining the original strong LSPR properties remains a significant challenge.

In this study, we developed a simple and efficient synthetic method to produce a AuNBPs-based trimetallic nanostructure, which exhibited significantly enhanced photocatalytic performance compared to the monometallic AuNBPs. The synthesis of the trimetallic nanostructure involved the initial seed-mediated growth of AuNBPs, followed by further purification using a depletion flocculation method to obtain highly pure colloidal AuNBPs. Subsequently, a hydrothermal method was employed to reduce the precursors of silver and platinum on the surface of the AuNBPs, forming a silver–platinum alloy shell. For photocatalytic tests, we employed a borohydride reduction method under illumination to reduce the MO dye, and the spectral changes in the solution during the reaction were monitored using a UV–vis spectrophotometer to assess the

reaction progress. In the experiments, photocatalysis were performed using different types of nanoparticles, and the synthesized trimetallic nanostructure, AuNBP@AgPt nanoparticles, exhibited the most significant enhancement in photocatalytic performance.

2. RESULTS AND DISCUSSION

The choice to use AuNBPs was motivated by their sharply pointed ends. In comparison to AuNRs, which have circular or flattened ends, AuNBPs exhibit stronger local electric field enhancement, more pronounced LSPR peaks, narrower full width at half-maximum (fwhm), better shape and size consistency, and higher refractive index sensitivity. Additionally, the spectral range of AuNBPs can be tuned within the range of approximately 600 to 1100 nm.

In the experiments, we employed a seed-mediated growth method to synthesize AuNBPs with certain modifications in some details. In brief, we subjected the seeds to heat treatment and introduced them into the growth solution for overnight growth, resulting in a solution of AuNBPs. The obtained solution was further purified by the depletion flocculation method, finally yielding AuNBPs with a purity exceeding 98%. The UV-vis-NIR spectra and the transmission electron microscopy (TEM) images of the AuNBPs before and after purification are shown in Figure S1. The final purified AuNBPs exhibited an LSPR peak at 725 nm with an average length of 83.2 ± 4.5 nm and an average width at the widest point of 28.4 ± 1.8 nm.

For the synthesis of trimetallic structures, we introduced AgNO_3 , K_2PtCl_4 , and ascorbic acid (AA) into the AuNBPs solution, followed by a hydrothermal reaction, resulting in a AuNBP@AgPt core-shell trimetallic structure. By adjusting the amounts of AgNO_3 and/or K_2PtCl_4 , as well as the type, ratio, and amount of surfactant used in the reaction, we have successfully synthesized a series of trimetallic structures with varying surface roughness (Figure 1). From this series, we

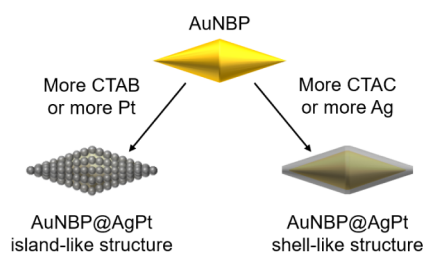


Figure 1. Schematic diagram illustrates the experimentally synthesized AuNBPs and two different morphologies of AuNBP@AgPt core-shell trimetallic nanostructures. The bottom-left image represents the AuNBP@AgPt island-like core-shell trimetallic structure obtained by using more CTAB or more Pt during synthesis; while the bottom-right image represents the AuNBP@AgPt shell-like core-shell trimetallic structure obtained by using more CTAC or more Ag during synthesis.

selected a representative group of particles, with the LSPR peak positioned at 724 nm, an average length of 86.5 ± 5.2 nm, and an average width at the widest point of 36.5 ± 2.7 nm.

In the experiments, we observed that surfactants CTAB and CTAC played important roles in controlling and promoting the growth of Pt and Ag, respectively. To understand the impact of these surfactants on the final nanostructures, we adjusted the ratio of these two surfactants in the solution

during the growth of silver-platinum alloy on the surface of AuNBPs. This led to the formation of a series of trimetallic structures with completely different growth patterns.

Figure 2 presents the UV-vis-NIR spectra for different proportions of CTAB in the surfactant, including 100%, 75%, 50%, 25%, and 0%, along with corresponding images depicting the changes in the spectral peak positions and intensities. Additionally, transmission electron microscope (TEM) images for three scenarios with CTAB proportions of 100%, 50%, and 0% are shown, along with high-resolution TEM (HRTEM) and energy-dispersive X-ray spectroscopy (EDS) elemental mapping images for the case with a 50% CTAB proportion. Detailed TEM images, HRTEM images, and EDS elemental mapping images can be found in Figures S2 and S3.

From the spectra (Figure 2a,b), we observed that when CTAB constituted 100% of the added surfactant, the spectrum experienced a certain degree of redshift and the intensity decreased significantly after the growth of silver-platinum alloy on the surface of AuNBPs. As the CTAC content increased and CTAB content decreased, the spectra gradually exhibited blueshift, and the intensity increased, continued until CTAB constituted 0%, that is CTAC comprised 100% of the surfactant, resulting in the maximum blueshift in the spectrum, however, the intensity of the spectrum decreased while CTAB constituted 0%.

From the TEM images (Figures 2c-e and S2b-f), we can also observe that when the CTAB content is higher, the growth of the silver-platinum alloy particles tends to be more island-like. In contrast, when the CTAC content is higher, the growth on the particle surface tends to be more shell-like. Moreover, when CTAC constitutes 100% of the surfactant, the alloy shell on the particle surface exhibits a high level of smoothness. Similarly, we measured the particle sizes in the TEM images. In Figure 2c, the shell thickness of the nanoparticles (i.e., the diameter of the particulate AgPt alloy) is 7.1 ± 0.9 nm. In Figure 2d, the shell thickness of the nanoparticles (i.e., the diameter of the particulate AgPt alloy) is 7.5 ± 1.0 nm. In Figure 2e, the shell thickness of the nanoparticles is 9.0 ± 0.7 nm.

To understand the elemental distribution and crystalline structure of the AuNBP@AgPt nanostructure, we selected nanoparticles under three conditions: CTAB comprises 100%, 50%, and 0% of the surfactant for HRTEM and EDS elemental analysis. In the EDS energy spectrum, Au, Ag, and Pt are colored yellow, blue, and red, respectively.

From the HRTEM images (Figures 2f and S2g-i), when CTAB constitutes 100%, the AgPt alloy grows in an island-like pattern on the surface of AuNBP, where the core's lattice spacing of 2.05 Å is close to the lattice spacing of the Au(100) crystal plane at 2.04 Å, and the lattice spacing of the island-like shell at 1.96 Å matches that of the Pt(100) crystal plane at 1.96 Å. When CTAB constitutes 50%, the AgPt alloy still grows in an island-like manner, but the size of the islands is slightly larger compared to the previous scenario. The core's lattice spacing of 2.01 Å is close to the Au(100) crystal plane at 2.04 Å, and the lattice spacing of the island-like shell at 2.30 Å falls between the lattice spacing of the Pt(111) crystal plane at 2.26 Å and the Ag(111) crystal plane at 2.36 Å. When CTAB constitutes 0%, a smooth AgPt alloy shell forms on the surfaces of AuNBP particles. The core's lattice spacing of 2.35 Å matches the Au(111) crystal plane at 2.35 Å, and the lattice spacing of the island-like shell at 2.36 Å matches the Ag(111) crystal plane at 2.36 Å.

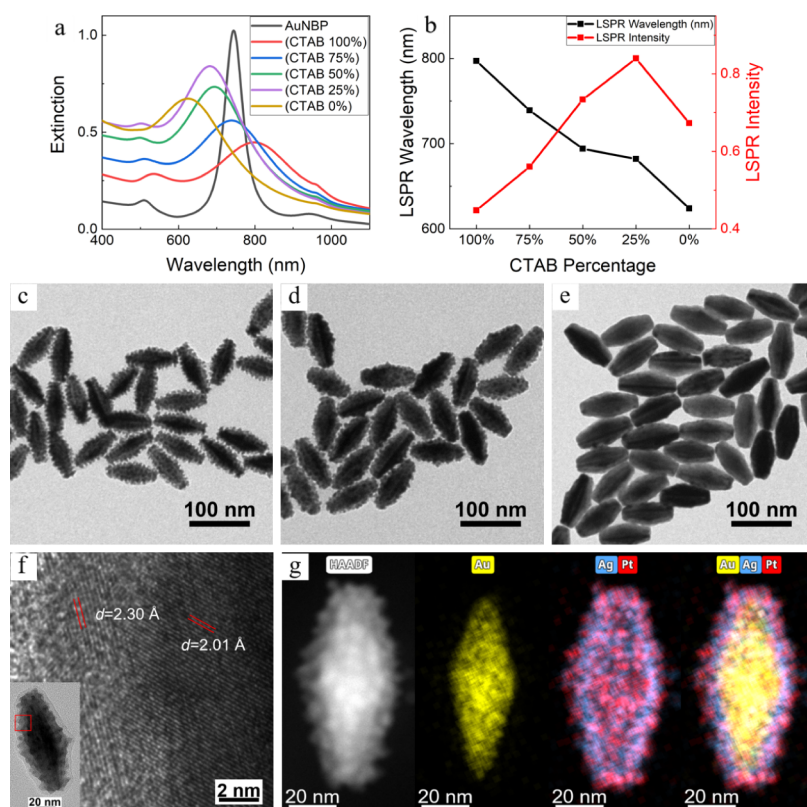


Figure 2. Morphology control of AuNBP@AgPt trimetallic nanostructures by adjusting the type and amount of surfactants. (a,b) UV–vis–NIR spectra of AuNBP@AgPt trimetallic nanoparticles synthesized under five different conditions with varying CTAB proportions (100%, 75%, 50%, 25%, and 0%), along with corresponding LSPR peak positions and intensities variations. (c,d,e) TEM images of the AuNBP@AgPt nanoparticles synthesized under three different conditions with CTAB proportions of 100% (c), 50% (d), and 0% (e). (f) HRTEM image of the AuNBP@AgPt nanoparticles synthesized with a 50% CTAB proportion. (g) HAADF-STEM and EDS elemental mapping images of AuNBP@AgPt nanoparticles synthesized with a 50% CTAB proportion.

From the EDS energy spectrum (Figure S3), we can also observe that the elemental distribution of Ag and Pt completely overlaps; therefore, we can conclude that the surface growth on AuNBP particles is indeed a silver–platinum alloy. According to the data obtained from EDS, when CTAB constitutes 100%, the proportion of platinum in the silver–platinum alloy is approximately 40%; when CTAB constitutes 50%, the proportion of platinum is about 17%; when CTAB constitutes 0%, the proportion of platinum is around 16%. However, the ratio of silver to platinum precursor added in the experiment is 5:1. Theoretically, the proportion of platinum in the silver–platinum alloy should be 16.7%. However, when CTAB accounts for 100%, the proportion of platinum in the shell is 40%, significantly higher than the theoretical value. Conversely, when CTAB accounts for 50% and 0%, the proportions of platinum in the shell (17% and 16%, respectively) are close to the theoretical value.

Following this, we supplemented the ICP test results for a group of AuNBP@AgPt nanoparticles with varied surfactant types and ratios. The detailed results are presented in Table S1. From the table, it can be observed that the silver content relative to gold increases as the amount of CTAB decreases, while the platinum content relative to gold remains largely unchanged, except for a significant increase when the CTAB content is at 0%. The reasons for these results will be further discussed in the subsequent text.

To investigate the surface elemental composition of AuNBP@AgPt particles, we performed X-ray photoelectron

spectroscopy (XPS) on AuNBP@AgPt with 50% CTAB. From the XPS spectra in Figure S4, it can be observed that the Au spectrum exhibits two peaks at 87.18 and 83.48 eV, corresponding to Au 4f_{5/2} (87.7 eV) and Au 4f_{7/2} (84.0 eV). The Ag spectrum shows two peaks at 373.48 and 367.48 eV, corresponding to Ag 3d_{3/2} (374.3 eV) and Ag 3d_{5/2} (368.3 eV). The Pt spectrum displays four peaks at 74.58, 73.48, 71.48, and 70.18 eV. According to the standard peaks for Pt, there should only be two peaks: Pt 4f_{5/2} (74.6 eV) and Pt 4f_{7/2} (71.2 eV). We hypothesize that the sample underwent a certain degree of oxidation, causing the peak shifts.

The experimental data deviated from this expectation, and we have several interpretations for this. First, the reduction potential of Ag⁺ is lower than that of Pt²⁺. Therefore, when AA is introduced into an aqueous solution of AgNO₃ and K₂PtCl₄, the reaction will preferentially occur with K₂PtCl₄. Even if Ag atoms are generated, they will gradually be oxidized back to Ag⁺ ions, and the resulting electrons will quickly be captured by Pt²⁺ ions, forming Pt atoms through the reduction process. Second, this is related to the Br[−] ions in CTAB. Theoretically, AgBr has a lower solubility in water than AgCl, which will partially inhibit the reaction of Ag⁺. Therefore, when CTAB is used as the surfactant, Br[−] ions significantly inhibit the reaction of Ag⁺ ions, resulting in a lower silver content in the shell of the synthesized nanoparticles. When CTAC is used as the surfactant, Ag⁺ ions are not significantly influenced by elements like Br[−] ions that drastically reduce the concentration of Ag⁺ ions in the solution. Additionally, since the concentration of

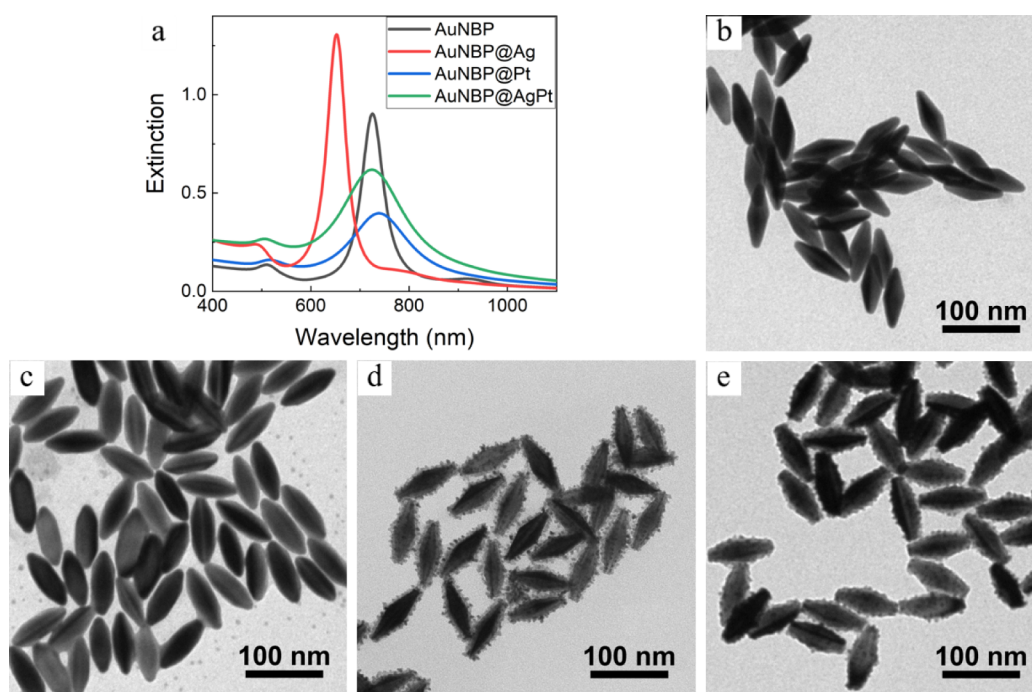


Figure 3. Morphologies of AuNBP nanoparticles and their surface coating with different metals. (a) UV-vis-NIR spectra of AuNBP nanoparticles, AuNBP@Ag bimetallic nanoparticles, AuNBP@Pt bimetallic nanoparticles, and AuNBP@AgPt trimetallic nanoparticles. (b–e) TEM images of nanoparticles of AuNBP (b), AuNBP@Ag (c), AuNBP@Pt (d), and AuNBP@AgPt (e).

AgNO_3 in the solution is five times that of K_2PtCl_4 , the resulting nanoparticles will have a significantly higher silver content in their shells.

Based on the various data and observations mentioned above, we believe that CTAB is more conducive to the reduction and growth of Pt during synthesis, leading to an elevated proportion of Pt in the silver–platinum alloy; the lattice in the alloy is dominated by Pt, due to the mismatch in lattice constants between Au (4.08 Å) and Pt (3.92 Å); this results in the island-like growth of the silver–platinum alloy on the surface of AuNBP particles, forming a granular structure. On the other hand, CTAC plays a role in promoting the reduction and growth of Ag during synthesis, leading to an increased proportion of Ag in the silver–platinum alloy; in this case, the lattice in the alloy is dominated by Ag; since the lattice constants of Au (4.08 Å) and Ag (4.09 Å) are close, the silver–platinum alloy grows epitaxially on the surface of AuNBP particles, forming a shell-like alloy layer. In subsequent experiments, we prioritized the experimental group with 50% CTAB as the main research subject.

To compare the catalytic performance, we synthesized individual AuNBP@Ag and AuNBP@Pt bimetallic nanoparticles and compared them with trimetallic nanoparticles and AuNBP. The UV-vis-NIR spectra and TEM images of AuNBP, AuNBP@Ag, AuNBP@Pt, and AuNBP@AgPt nanoparticles are shown in Figure 3.

From the spectra (Figure 3a), it can be observed that after the surface growth of Ag on the AuNBP, the LSPR peak intensity increases, and the peak position undergoes a blue shift; this is because, compared to Au, Ag has a higher plasmonic resonance energy and smaller plasmonic damping. However, after the surface growth of Pt, the LSPR peak intensity significantly decreases, and the peak position slightly red-shifts, this is attributed to the large imaginary part of the dielectric function of Pt, leading to significant plasmonic

damping. For the AuNBP@AgPt trimetallic nanoparticles synthesized in this experiment, the LSPR peak intensity slightly decreases, and the peak position is close to that of the original AuNBP. The main difference compared to the AuNBP is that the LSPR peak becomes broader, which is a result of the interaction between the strong plasmon resonance of Ag and the strong plasmonic damping of Pt.

According to the TEM images (Figure 3b–e), it can be observed that when the surface of AuNBP is coated with Ag, the growth of the silver shell tends to form a smooth shell structure, creating a smooth outer shell on the surface of AuNBP. On the other hand, when Pt is grown on the surface of AuNBP, Pt tends to grow in an island-like fashion, resulting in an irregular and rough shell. Similarly, we measured the particle sizes in the TEM images. In Figure 3c, the shell thickness of the nanoparticles is 4.3 ± 1.2 nm. In Figure 3d, the shell thickness of the nanoparticles is 2.7 ± 1.7 nm. In Figure 3e, the shell thickness of the nanoparticles is 7.4 ± 1.3 nm.

The factors influencing different growth modes are manifold. They include differences in lattice structures between the core and shell, disparities in solid–vapor surface free energy (E_S) among different metals, and variations in bond dissociation energy (E_D) between metals.⁶⁰ In simple terms, if the E_S of the shell is smaller than that of the core, then the lower interfacial energy favors wetting of the core by the shell metal, making continuous growth more likely. Additionally, when the E_D between atoms of the core and shell metals is greater than that between atoms of the shell metal itself, continuous growth of the shell is more probable. The occurrence of epitaxial growth depends to some extent on the lattice parameters of the core and shell metals, as well as the thickness of the shell. When the lattice constants of the core and shell metals are similar, the shell metal is more likely to undergo epitaxial growth on the core. Conversely, when there is a significant difference in the

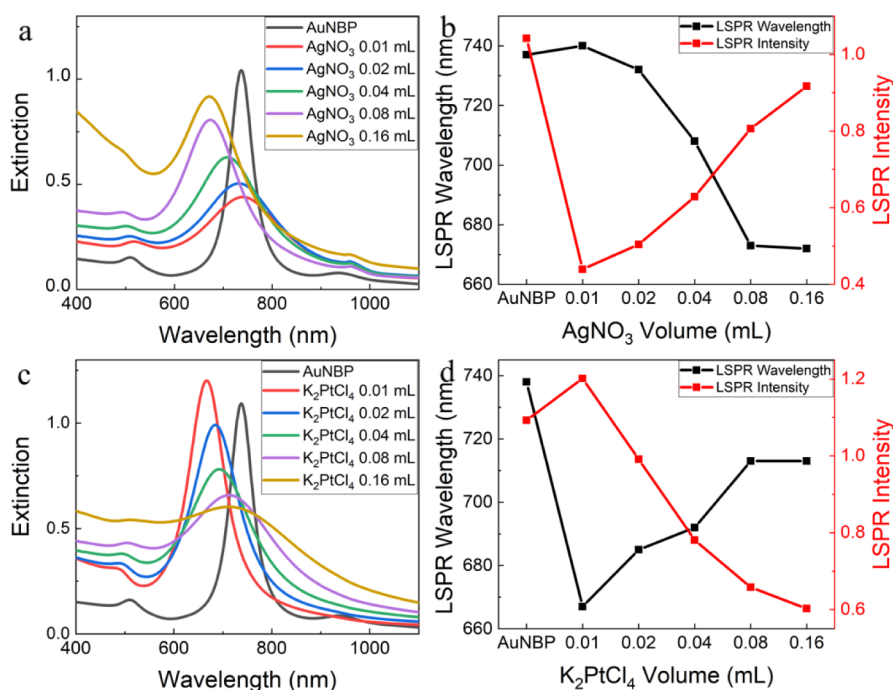


Figure 4. Morphologies of AuNBP@AgPt trimetallic nanoparticles by adjusting the amounts of AgNO₃ and K₂PtCl₄. (a,b) UV–vis–NIR spectra and corresponding LSPR peak positions and intensities of AuNBP@AgPt trimetallic nanoparticles synthesized by adjusting the amounts of AgNO₃ (0.01–0.16 mL, 0.01 M). (c,d) UV–vis–NIR spectra and corresponding LSPR peak positions and intensities of AuNBP@AgPt trimetallic nanoparticles synthesized by adjusting different amounts of K₂PtCl₄ (0.01–0.16 mL, 0.002 M).

lattice constants between the core and shell metals, epitaxial growth is still possible as long as the shell is thin enough.

The conclusions drawn from the analysis above align with the findings derived from the analysis of HRTEM images when the surfactant. The lattice constants of Au (4.08 Å) and Ag (4.09 Å) are similar, and the E_s of Ag (1.24 J/m²) is less than that of Au (1.50 J/m²), while the E_D of Ag–Au (203 kJ/mol) is greater than that of Ag–Ag (160 kJ/mol), leading to a shell-like growth of Ag on the surface of AuNBP. However, the lattice constants of Au (4.08 Å) and Pt (3.92 Å) do not match, and the E_s of Pt (2.49 J/m²) is greater than that of Au (1.50 J/m²), while the E_D of Pt–Pt (307 kJ/mol) is greater than that of Au–Au (226 kJ/mol), resulting in island-like growth of Pt on the surface of AuNBP. When growing AgPt alloy on the surface of AuNBP, the alloy growth exhibits a distinct core–shell structure, including irregular and rough surfaces with island-like growth. This morphology seems to be more favorable for increasing the surface area, enhancing the catalytic activity.

In the experiments, we also attempted to influence the final nanostructure by controlling the concentrations of precursors AgNO₃ and/or K₂PtCl₄. While maintaining the CTAB ratio at 50%, we conducted experiments with different amounts of AgNO₃ (0.01–0.16 mL, 0.01 M) and K₂PtCl₄ (0.01–0.16 mL, 0.002 M). The UV–vis–NIR spectra for all samples, along with the corresponding LSPR peak positions and intensities, are depicted in Figure 4. The corresponding TEM images can be found in Figures S5 and S6.

Figure 4a shows the UV–vis–NIR spectra of AuNBP@AgPt nanostructures with different amounts of AgNO₃ (0.01–0.16 mL, 0.01 M), while keeping the K₂PtCl₄ constant (0.04 mL, 0.002 M). Figure 4b shows the corresponding LSPR peak positions and intensities. With the increase in AgNO₃ concentration, the LSPR underwent a blue shift and the intensity increases. This is due to the fact that compared to Au,

Ag material has a higher plasmon resonance energy and smaller plasmon damping. From Figure S5b–f, when 0.01 mL of AgNO₃ was used, Pt formed particles on the surface of AuNBP, creating a AuNBP@AgPt island heterostructure. As the amount of AgNO₃ increases, the surface gradually forms a fully covered continuous shell, but the shell surface remains uneven with noticeable roughness. When the amount of AgNO₃ was increased to 0.16 mL, a smooth alloy shell of AgPt was eventually formed.

Similarly, the amount of K₂PtCl₄ also affected the final morphology of the AuNBP@AgPt nanostructures. In the experiments, we added K₂PtCl₄ from 0.01 to 0.16 mL (0.002 M), while keeping the amount of AgNO₃ fixed (0.04 mL, 0.01 M). Figure 4c displays the UV–vis–NIR spectra of AuNBP@AgPt nanoparticles with varying amounts of K₂PtCl₄. Figure 4d shows the corresponding LSPR peak positions and intensities. It can be observed that with the increase in K₂PtCl₄ concentration, the LSPR red-shifted and broadened, and the intensity gradually decreased. This is due to the significant plasmon damping caused by the large imaginary part of the dielectric function of Pt material. Therefore, different structures could be obtained by simply adjusting the quantities of AgNO₃ and/or K₂PtCl₄ precursors. The TEM images are shown in Figure S6. With the increase in K₂PtCl₄ content, the outer layer begins as a smooth shell structure and gradually transitions to a dendritic structure (K₂PtCl₄ > 0.04 mL). Further increasing the amount of K₂PtCl₄ makes the dendritic structure more pronounced.

In our experiments, we directly deposited a silver–platinum alloy on the surface of AuNBP. Depending on the different surfactants or the amount of added Ag and Pt precursors, different morphologies could be formed. In the experiment involving surfactant variation, we added an excess of reducing agent AA. Theoretically, all Ag and Pt precursors would be

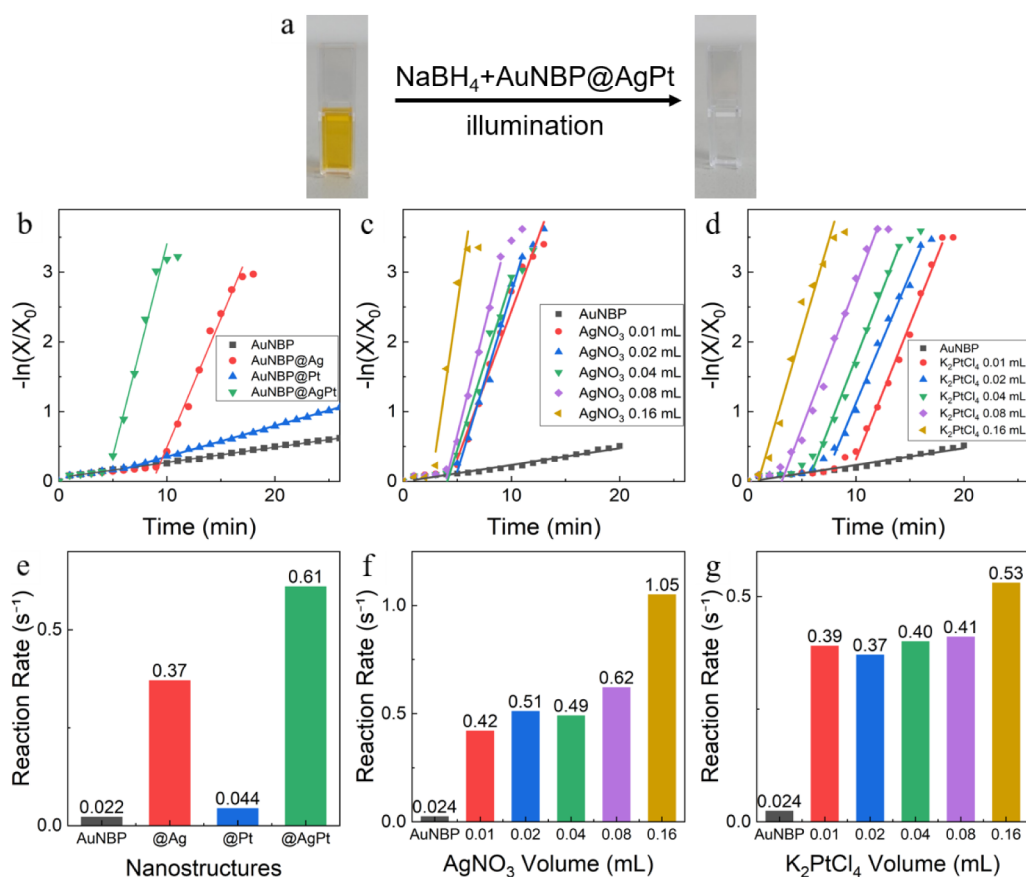


Figure 5. Plasmon-enhanced photocatalytic performance of different nanostructures of AuNBP@AgPt. (a) Schematic representation of the MO reduction process under Xe lamp irradiation using NaBH₄, with the color of the solution changing from yellow to colorless. (b,e) The scatter plot of the photocatalytic performance process and rate (slope) bar chart of AuNBP@AgPt nanoparticles with different metal coatings. (c,f) The scatter plot of the photocatalytic performance process and rate (slope) bar chart of AuNBP@AgPt nanoparticles with varying amounts of AgNO₃ in the experiment. (d,g) The scatter plot of the photocatalytic performance process and rate (slope) bar chart of AuNBP@AgPt nanoparticles with varying amounts of K₂PtCl₄ in the experiment.

reduced to atoms and deposited on AuNBP, resulting in a silver–platinum alloy with a Pt ratio of 16.7%. However, the experimental data deviated from this expectation, and we have several points of view on this matter. First, the reduction potential of Ag⁺ is lower than that of Pt²⁺, so when AA was introduced into the AgNO₃ and K₂PtCl₄ aqueous solution, the reaction would preferentially occur on K₂PtCl₄, even if Ag atoms were generated, they would gradually be oxidized to Ag⁺ ions, and the generated electrons were rapidly captured by Pt²⁺ ions through the reduction process to form Pt atoms. Second, this is related to the bromide ions (Br⁻) in CTAB. Theoretically, AgBr is less soluble in water than AgCl, which would suppress the reaction of Ag⁺ to some extent, leading to a lower Ag content in the shell of the CTAB group.

The entire reaction process was summarized as follows: The precursors AgNO₃ and K₂PtCl₄ are coreduced by AA to form Ag and Pt atoms. The generated Ag and Pt atoms codeposit on AuNBP, forming an AgPt alloy shell. When CTAB is used as the surfactant, bromide ions (Br⁻) to some extent suppress the reaction of Ag⁺ ions, causing Pt to be preferentially reduced. During the deposition on the surface of AuNBP, due to the mismatch in lattice constants, there is a tendency for island-like growth, ultimately resulting in a granular AgPt alloy shell. When CTAC is used as the surfactant, Ag and Pt are reduced almost simultaneously. Since Ag constitutes the majority, during the deposition on the surface of AuNBP, the lattice of

the AgPt alloy is dominated by Ag. Because the lattice constants of Ag and Pt are close, an epitaxial growth occurs, forming a complete shell-like structure.

To investigate the photocatalytic activities of AuNBP@AgPt trimetallic nanostructures under plasmonic enhancement, we chose the reduction of the MO solution using NaBH₄ as the model reaction system and conducted experiments under xenon lamp irradiation. During the reduction process, the color of the MO solution changes from orange to colorless.

During the photocatalytic reactions, we measured and recorded the intensity of the characteristic absorption peak of the MO solution at a wavelength of 463 nm in the visible–near-infrared spectrum as a function of reaction time. This was done to reflect the photocatalytic rate. The experimental procedure is illustrated in Figure 5a. Specifically, at the beginning of the reaction ($t = 0$ min), we determined the peak value X_0 of the MO solution, and then, at appropriate time intervals during the reaction (1 or 2 min), we measured the peak value X_i at the wavelength of 463 nm. Subsequently, we calculated the $-\ln(X_i/X_0):t$ curve, the fast-rising phase of the curve was linearly fitted, and the slope of the fitted line was taken as the standard for the reaction rate. Specific representations of the photocatalytic performance process and rate (slope) bar charts are shown in Figures 5 and S7.

Figure S7a presents the reaction process for the trimetallic nanostructures obtained by changing the type and amount of

surfactant as catalysts. The catalytic rates of AuNBPs under the same conditions were used as a control, and the catalytic rates of different morphologies of nanoparticles were calculated, with the catalytic rates presented in the bar chart in Figure S7b and the specific catalytic rates recorded in Table S2. The raw data for photocatalysis are shown in Figure S8. It could be observed that although there is not a significant change in the catalytic rates among the trimetallic nanostructures obtained by altering the type and amount of surfactant, a trend of initially increasing and then decreasing is evident. Moreover, all these rates are significantly higher than that of AuNBPs under the same conditions. When both types of surfactants were present simultaneously, there is a slight improvement in the catalytic performance of the synthesized trimetallic nanostructures.

Figure 5b illustrates the scatter plot of the photocatalytic reaction processes of AuNBP, AuNBP@Ag, AuNBP@Pt, and AuNBP@AgPt nanoparticles as catalysts. The catalytic rates of AuNBPs under the same conditions were used as a control, and the catalytic rates of different morphologies of nanoparticles were calculated, with the catalytic rates presented in the bar chart in Figure 5e, and the specific catalytic rates recorded in Table S3. The raw data for photocatalysis are shown in Figure S9. Among these four types of metallic nanostructures, AuNBP@AgPt exhibits the highest catalytic rate, being 27.8 times higher than the catalytic rate of AuNBPs under the same conditions.

Figure 5c depicts the scatter plot of the reaction process of AuNBP@AgPt nanostructures as catalysts under different amounts of AgNO_3 (0.01 to 0.16 mL, 0.01 M) while keeping K_2PtCl_4 constant (0.04 mL, 0.002 M). The catalytic rates of AuNBP under the same conditions were used as a control, and the catalytic rates of different morphologies of nanoparticles were calculated with the catalytic rates presented in the bar chart in Figure 5f, and the specific catalytic rates recorded in Table S4. The raw data for photocatalysis are shown in Figure S10. It could be observed that changing the AgNO_3 alters the catalytic rates of AuNBP@AgPt nanostructures. When AgNO_3 is 0.01 mL, the relative rate was 17.8 times higher; with an increase in AgNO_3 , the catalytic rate of AuNBP@AgPt nanoparticles gradually increased. When AgNO_3 is increased to 0.16 mL, the relative rate also increases 44.0 times.

In Figure 5d, while keeping AgNO_3 constant (0.04 mL, 0.01 M), the scatter plot of the reaction process is presented when K_2PtCl_4 is added from 0.01 to 0.16 mL (0.002 M) for AuNBP@AgPt nanostructures as catalysts. Similar to the previous condition, the catalytic rates of AuNBP under the same conditions were used as a control, the catalytic rates of different morphologies of nanoparticles were calculated, with the catalytic rates presented in the bar chart in Figure 5g, and the specific catalytic rates were recorded in Table S5. The raw data for photocatalysis are shown in Figure S11. Changing K_2PtCl_4 had a minimal impact on altering the catalytic rates of AuNBP@AgPt nanostructures. When K_2PtCl_4 is 0.01 mL, the relative rate was 16.1 times higher; with an increase in K_2PtCl_4 , the catalytic rate of AuNBP@AgPt nanoparticles remain relatively constant. When K_2PtCl_4 is increased to 0.16 mL, the relative rate slightly increases 21.9 times. However, it is observed that although the amount of K_2PtCl_4 had a minimal effect on the photocatalytic rate, it did influence the initiation time of the catalysis by AuNBP@AgPt nanoparticles. When K_2PtCl_4 is 0.01 mL, the photocatalytic reaction of AuNBP@AgPt nanoparticles takes about 10 min to initiate. With an

increase in K_2PtCl_4 , the initiation time gradually shortens, and when K_2PtCl_4 is increased to 0.16 mL, the reaction initiates in approximately 2 min. It can be concluded that the presence of Pt significantly reduces the initial time.

In our photocatalytic experiments, two main conditions influence the catalytic rate: the type of catalytic particles, which refers to the different types of nanoparticles we synthesized, and the volume and concentration of the added components, including methyl orange, catalytic particles, and NaBH_4 . For methyl orange, we prepared a large amount of 0.15 mM solution and used 1 mL for each photocatalytic experiment, ensuring a consistent concentration and volume. NaBH_4 is easily oxidized in air, so we prepared it in a consistent manner each time to maintain its reducing properties. We also analyzed the data for each set of experiments using the catalytic rate of AuNBP as a baseline to calculate the relative rates of other multimetallic nanoparticles within the same group, thereby minimizing the impact of NaBH_4 concentration variability. Regarding the concentration of nanoparticles, we first centrifuged and washed the synthesized nanoparticles twice and then reconstituted them to the original volume before washing. Figure S12 shows the spectra of a set of AuNBP@AgPt nanoparticles with varied surfactant components before and after washing, with solid lines representing the spectra before washing and dashed lines representing the spectra after washing. From the spectra, it can be seen that both AuNBP and AuNBP@AgPt experienced some loss after washing. However, data analysis indicates that the nanoparticles retained 90% to 93% of their original intensity after washing. Given that the differences in experimental results are significantly greater than 3%, we believe that this washing procedure is effective and ensures the accuracy of the experimental results.

To demonstrate the presence of the plasmonic enhancement effect provided by AuNBP, we conducted catalytic experiments on both AuNBP and AuNBP@AgPt nanoparticles under illuminated and nonilluminated conditions. The experimental procedure was identical with the photocatalytic experiment, with the only difference being the absence of illumination. The results of these experiments are shown in Figure S13. By comparing the catalytic performance under illuminated and nonilluminated conditions, we can confirm the presence of the plasmonic enhancement effect provided by AuNBP. Additionally, by comparing the catalytic performance of AuNBPs with and without the silver–platinum alloy coating, we can demonstrate the catalytic effect of the silver–platinum alloy. According to the experimental results, AuNBPs alone exhibit negligible catalytic activity under dark conditions. Therefore, both the silver–platinum alloy shell under dark conditions and the plasmonic enhancement effect provided by illumination contribute to enhanced catalytic performance.

Based on the results above, we believe that the catalytic performance of platinum (Pt) mainly arises from its intrinsic chemical catalytic ability, while the catalytic abilities of gold (Au) and silver (Ag) primarily stem from their plasmonic enhancement effects. Therefore, when we coat the nanoparticle surface with silver, the presence of silver significantly enhances the nanoparticle's plasmonic properties. Moreover, when we alter the silver content, significant changes occur in the nanoparticle's plasmonic properties, as evidenced by the spectral changes observed when varying the silver content. Conversely, when we coat the nanoparticle surface with platinum, the platinum content constitutes only a small proportion, and thus, its intrinsic chemical catalytic perform-

ance does not play a significant role. In the trimetallic nanoparticles, introducing both silver and platinum allows silver to act as a plasmonic enhancer, while the platinum nanoparticles on the surface serve as high-performance catalytic hotspots, effectively utilizing the plasmonic excitation induced by silver. When we vary the platinum content, the amount of excited plasmon does not change significantly because the silver content remains constant. However, as the platinum content increases, electron exchange in the silver–platinum alloy becomes more frequent and the contact area between platinum and the solution increases. Under these combined factors, the reaction initiation time gradually decreases with an increase in the platinum content.

To test the reusability of the catalyst, we conducted cyclic photocatalysis experiments on the AuNBP@AgPt nanoparticles. Considering reaction time and rate, we chose to use AuNBP@AgPt synthesized by adding 0.04 mL AgNO₃ and 0.04 mL K₂PtCl₄ for the cyclic photocatalysis experiments. Ten photocatalytic cycles were performed with centrifugation twice at the end of each cycle for collecting and cleaning the catalyst. Experimental results (Figure S14) indicated that after 10 cycles, the catalytic efficiency of AuNBP@AgPt still remains at an exceptionally high level. After 10 rounds of photocatalysis, we measured the extinction spectrum of the AuNBP@AgPt sample and conducted TEM imaging, as shown in Figure S14. The raw data for photocatalysis are shown in Figure S15. It is noteworthy that there is no significant difference in the spectra before and after 10 cycles, except for a slight decrease in intensity, which can be attributed to some loss during the centrifugation. The TEM images show that the nanostructure of AuNBP@AgPt undergoes no significant changes after 10 cycles of photocatalysis.

Based on the above data, AuNBP@AgPt synthesized by us demonstrates promising potential for recycling and reuse. Moreover, its catalytic activity can be directly stimulated by sunlight, offering the possibility of cost savings, particularly in terms of cost and power consumption in large-scale industrial applications. Therefore, the AuNBP@AgPt catalyst is expected to provide an economical solution for practical catalytic reactions.

In order to understand the reason behind the excellent performance of AuNBP@AgPt in photocatalysis, we conducted finite-difference time-domain (FDTD) simulations to calculate the extinction spectra and electric field distribution at the catalytic interface of individual AuNBP@AgPt nanostructures.

In the FDTD simulations, we first modeled the AuNBP based on the dimensions obtained from experiments. As shown in Figure 6a, we utilized the rounded tip cone model from the built-in shapes in FDTD to create two back-to-back cones; each cone had a height of 40 nm, a bottom radius of 14 nm, a top radius of 4 nm, and a cone angle of 32°; this resulted in the basic AuNBP model we needed.

In our experiments, we synthesized a series of different nanostructures and established the corresponding models in FDTD simulations. Building on these models, we further created larger bipyramid models or numerous small sphere models as the metal shell layer of AuNBP. The shell layer has varying thicknesses in different structures. For example, Figure S16b depicts the model of AuNBP@Ag with a shell thickness of approximately 4 nm; Figure S16c shows the model of AuNBP@Pt with a shell thickness of about 2 nm. Figure S16d,e illustrates the rough surface models of AuNBP@AgPt, representing the condition with more CTAB, with a shell

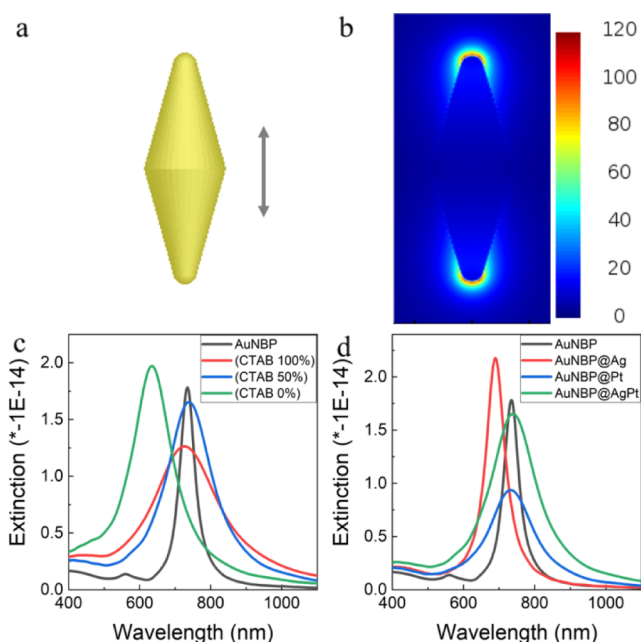


Figure 6. FDTD simulations of different nanostructures. (a) Model of AuNBP in the FDTD simulation software, with arrows indicating the direction of light oscillation. (b) Electric field distribution of a single AuNBP, with the hotspots located at the apex of the AuNBP, and the peak intensity is approximately 111. (c) FDTD simulations of the longitudinal LSPR extinction spectra of three types of AuNBP@AgPt nanoparticles obtained by adjusting the surfactants. (d) FDTD simulations of the longitudinal LSPR extinction spectra of AuNBP nanoparticles with different metal coatings.

thickness of around 7 nm. Figure S16f displays the smooth surface model of AuNBP@AgPt, representing the condition with less CTAB, with a shell thickness of about 9 nm.

For the electric field simulations in Figure 6b, the EM images presented correspond to the simulated spectra of AuNBP in Figure 6a at the LSPR peak wavelength (i.e., when the electric field enhancement is near its maximum intensity). Since the LSPR enhancement effect is the primary focus of our discussion, we aim to demonstrate the electric field enhancement at the LSPR peak intensity to substantiate its effect.

The simulated extinction spectra for the three particle types are shown in Figure 6c, exhibiting trends similar to those of the experimental data. Similarly, we modeled and simulated the AuNBP@Ag and AuNBP@Pt bimetallic nanoparticles. The results, shown in Figure 6d, closely approximate the experimental data. The simulation of the electric field for a single AuNBP is shown in Figure 6b. Additionally, we simulated the electric field distribution of AuNBP@AgPt, revealing enhanced electric fields at the two apexes of the bipyramid for both AuNBP and AuNBP@AgPt. More simulation results of the electric field can be found in Figure S16.

Therefore, we propose a possible plasmon-mediated photocatalytic mechanism. The gold nanobipyramids and Ag components absorb visible light through surface plasmon resonance (SPR), generating high-energy electrons. These electrons transfer to the Pt component via the alloy structure, facilitating charge separation and prolonging the lifetime of the electrons and holes, thus preventing recombination. The Pt surface catalyzes the reduction of oxygen to produce reactive oxygen species (ROS), such as superoxide anions and hydroxyl

radicals. These ROS attack and decompose MO molecules into smaller biodegradable compounds. Remaining holes can oxidize MO or water to generate additional hydroxyl radicals, further aiding in decomposition. The final decomposition products desorb from the catalyst surface, regenerating the active sites and allowing the catalytic cycle to continue. Additionally, Ag enhances the generation of hot electrons and transfers them to Pt in the AgPt alloy. The strong plasmonic resonance of Ag also counteracts the negative impact of Pt's plasmon damping, significantly reducing reaction time. Furthermore, the Au and Ag components, with their surface plasmon resonance characteristics, generate heat under illumination, raising the reaction temperature, thus increasing the reaction energy and enhancing the catalytic effect. The synergistic effects between the metals and the inherent catalytic activity of noble metals result in unique performance enhancements, with Pt's catalytic properties further boosted by the electric field generated by Au and Ag excitation.

3. CONCLUSIONS

We prepared AuNBP@AgPt trimetallic nanostructures using a simple and reproducible method. By adjustment of the type and amount of surfactants used during synthesis, as well as the amount of Ag and Pt precursors, the growth mode of the AgPt alloy shell can be controlled to form either island-like or shell-like structures. Both growth modes of AuNBP@AgPt trimetallic nanostructures exhibited excellent catalytic performance in the NaBH₄-assisted plasmon-mediated reduction of MO. Specifically, the reaction rate of the AuNBP@AgPt trimetallic nanostructures was 27.8 times higher than that of AuNBPs. Moreover, after 10 cycles of photocatalysis, it still maintained high catalytic activity, demonstrating excellent potential for recycling and reuse, which can significantly reduce costs in industrial applications and contribute to environmental protection. FDTD simulations confirmed that the hotspots in AuNBP@AgPt are located at the tip of AuNBP. The strong plasmonic effects of AuNBP itself contribute to its intense catalytic performance. Based on these results, we demonstrated the advantages of the experimentally synthesized AuNBP@AgPt trimetallic nanostructures in plasmon-mediated photocatalytic reactions. These structures serve as efficient photocatalysts, providing practical guidance for designing other plasmon-mediated photocatalysts and plasmon-enhanced devices in the future.

4. EXPERIMENTAL SECTION

4.1. Materials. All chemicals were used as received without further purification. Hexadecyltrimethylammonium bromide (CTAB, > 99.0%), L-ascorbic acid (AA, > 99.99%), chloroauric acid (HAuCl₄), hydrochloric acid (HCl, 37.0 wt % in water), and methyl orange (MO) were purchased from Macklin. Hexadecyltrimethylammonium chloride (CTAC, > 99.0%), sodium borohydride (NaBH₄, 98.0%), sodium citrate dihydrate (SC, 99.0%), silver nitrate (AgNO₃, > 99.8%), potassium tetrachloroplatinate (II) (K₂PtCl₄, > 99.99%), and benzyltrimethylhexadecylammonium chloride (HDBAC 95.0%) were purchased from Aladdin. Ultrapure water (Millipore Milli-Q grade) with a resistivity of 18.2 MΩ was used in all of the experiments. All glassware for the AuNBPs synthesis were cleaned with freshly prepared aqua regia (HCl/HNO₃ in a 3:1 volume ratio), rinsed with large amounts of water, and dried at 60 °C before usage.

4.2. Synthesis and Purification of AuNBPs. The AuNBPs samples were prepared by using a seed-mediated growth method. Briefly, a freshly prepared, ice-cold NaBH₄ solution (0.025 M, 0.25 mL) was added under vigorous stirring into an aqueous solution that

was premade by mixing together HAuCl₄ (0.01 M, 0.25 mL), SC (0.01 M, 5.0 mL), and CTAC (0.1 M, 5.0 mL). After a 2-min stirring period, transfer the seed solution into an 80 °C water bath and stir it slowly for 90 min. The color of the seed solution gradually changed from brown to red. Lastly, the seed solution was removed from the water bath and stored at room temperature. The seed solution (0.1 mL) was added into the growth solution, which consisted of CTAB (0.1 M, 20.0 mL), HAuCl₄ (0.01 M, 1.0 mL), AgNO₃ (0.01 M, 0.2 mL), HCl (1.0 M, 0.4 mL), and AA (0.1 M, 0.16 mL). This was followed by a gentle inversion mixing for 10 s. The mixed solution was left undisturbed overnight at 30 °C. To wash the AuNBPs, the solution was centrifuged at 8000 rpm for 10 min, and after removing the supernatant, the precipitate was dispersed in CTAB solution (1.5 mM, 6.0 mL). Subsequently, to purify AuNBP by removing impurity particles using the depletion flocculation method, a high concentration of HDBAC solution (0.5 M, 14.0 mL) was added, and the mixed solution was allowed to stand at 30 °C in a water bath for 24 h. Following this, the purple supernatant was carefully removed, and CTAB solution (1.5 mM, 5.0 mL) was added to the precipitate, which was then sonicated for 1 min to disperse the precipitate. The obtained purified solution (brown) was centrifuged at 8000 rpm for 10 min and washed with CTAB solution (1.5 mM, 5.0 mL), repeating this process twice to remove excess HDBAC. Finally, the purified AuNBP was dispersed in CTAB solution (1.5 mM, 1.0 mL) for subsequent experiments.

4.3. Synthesis of AuNBP@AgPt Trimetallic Nanostructures.

To deposit a silver–platinum alloy onto the surface of AuNBP, 0.05 mL of the purified AuNBPs solution was added to a mixed solution containing H₂O (2.4 mL), CTAB (0.1 M, 0.5 mL), and CTAC (0.1 M, 0.5 mL). The mixed solution was heated in a 60 °C water bath for 10 min. Subsequently, AA (0.1 M, 0.04 mL), AgNO₃ (0.01 M, 0.04 mL), and K₂PtCl₄ (0.002 M, 0.04 mL) were added to the solution and further heated for 60 min at 60 °C in the water bath. The obtained solution was centrifuged at 8000 rpm for 10 min and washed with H₂O. This process was repeated twice to remove impurities. Finally, the precipitate was dispersed in H₂O (1.0 mL) for subsequent experiments. To obtain AuNBP@AgPt nanostructures with different morphologies, we adjusted the amounts of AgNO₃ (from 0.01 to 0.16 mL), K₂PtCl₄ (from 0.01 to 0.16 mL), and the ratio of CTAB to CTAC (ranging CTAB from 100% to 0%). The detailed experimental parameters can be found in Tables S6–S10.

4.4. Characterizations. Optical extinction spectra were recorded using a UV-1900i spectrophotometer (Shimadzu, Japan) with a 10 mm optical path. TEM images were obtained with an HT-7700 microscope (Hitachi, Japan) operating at a voltage of 100 kV. HRTEM images and EDS mapping were performed using a Talos F200S TEM with a 200 kV acceleration voltage. The particle sizes of the nanoparticles were measured from TEM images using ImageJ software with measurements taken from more than 100 nanoparticles for each sample. ICP test data were obtained using a PerkinElmer NexION 2000 ICP-MS, and XPS data were acquired using a Thermo Scientific K-Alpha.

4.5. Photocatalysis. To perform the photocatalytic reactions, MO (0.15 mM, 1.0 mL) was mixed with freshly prepared NaBH₄ (0.1 M, 0.1 mL). Then, different kinds of AuNBP@AgPt (0.02 mL) or AuNBPs (0.02 mL) solutions were added to the mixture. These catalytic steps were performed under illumination with a 250 W xenon lamp (HDL-II, Suzhou Betic Optoelectronics Technology Co. Ltd., China). The MO concentration was determined at a wavelength of 465 nm using a UV–vis–NIR spectrophotometer (UV-1900i, Shimadzu). The extinction spectra were monitored at 1 min intervals until the 465 nm peak disappeared, and the color changed from orange to transparent. For the cycling test, the catalysts were obtained by centrifugation and redispersed in a MO/NaBH₄ system. The cycling test was carried out under the same conditions. For control experiments, we also conducted the catalytic reaction without light (dark), while keeping other conditions unchanged.

4.6. FDTD Simulations. Finite-difference time domain (FDTD) is a method for solving Maxwell's equations on a discretized spatial grid in complex geometries. The FDTD simulations were carried out

using commercial software (Ansys Lumerical FDTD). A total field scattered field source was used to simulate a propagating plane wave interacting with the nanostructures with a wavelength range of 300–1100 nm. A three-dimensional nonuniform mesh was used, and a grid size of 0.1 nm was chosen for calculating the spectra and electric field distributions of all nanostructures. For the dimensions, the average sizes as determined from TEM were used. The dielectric functions of Au were obtained by fitting the points from the data of Palik,⁶¹ and the dielectric function of Ag and Pt were obtained from the data of Rakic et al.⁶² We calculated the effective dielectric functions of the AgPt alloy by the effective medium approximation (EMA) based on the Maxwell–Garnett equation⁶³

$$\frac{\epsilon_{\text{eff}} - \epsilon_{\text{Ag}}}{\epsilon_{\text{eff}} + 2\epsilon_{\text{Ag}}} = P \frac{\epsilon_{\text{Pt}} - \epsilon_{\text{Ag}}}{\epsilon_{\text{Pt}} + 2\epsilon_{\text{Ag}}} \quad (1)$$

Thus, the effective dielectric functions of AgPt alloy are given by

$$\epsilon_{\text{eff}} = \epsilon_{\text{Ag}} \frac{2P(\epsilon_{\text{Pt}} - \epsilon_{\text{Ag}}) + \epsilon_{\text{Pt}} + 2\epsilon_{\text{Ag}}}{2\epsilon_{\text{Ag}} + \epsilon_{\text{Pt}} - P(\epsilon_{\text{Pt}} - \epsilon_{\text{Ag}})} \quad (2)$$

where ϵ_{Pt} , ϵ_{Ag} , and ϵ_{eff} are the dielectric functions of Pt, Ag, and the composite system (AgPt alloy), respectively. P is the proportion of Pt in the AgPt alloy that could be obtained from the EDS mapping. After calculating ϵ_{eff} it was imported into the FDTD software. The real and imaginary parts of ϵ_{eff} are plotted in Figure S17.

■ ASSOCIATED CONTENT

SI Supporting Information

The Supporting Information is available free of charge at <https://pubs.acs.org/doi/10.1021/acsnm.4c02124>.

Additional UV–vis–NIR spectra, TEM images, HRTEM images, EDS elemental mapping images, ICP test data, XPS spectra, raw data and computationally fitted data for the photocatalytic performances, FDTD simulation results, dielectric function of the AgPt alloy, and specific experimental parameters for synthesizing nanoparticles (PDF)

■ AUTHOR INFORMATION

Corresponding Author

Tian-Song Deng – School of Electronics and Information Engineering, Hangzhou Dianzi University, Hangzhou 310018, PR China; orcid.org/0000-0002-0841-4932; Email: dengts@pku.edu.cn

Authors

Er-Ji Zhang – School of Electronics and Information Engineering, Hangzhou Dianzi University, Hangzhou 310018, PR China; orcid.org/0009-0008-2829-7658

Yu-Chun Cheng – School of Electronics and Information Engineering, Hangzhou Dianzi University, Hangzhou 310018, PR China

Li-Yong Liu – School of Electronics and Information Engineering, Hangzhou Dianzi University, Hangzhou 310018, PR China

Jia-Fei Gao – School of Electronics and Information Engineering, Hangzhou Dianzi University, Hangzhou 310018, PR China

Jiahong Wen – School of Electronics and Information Engineering, Hangzhou Dianzi University, Hangzhou 310018, PR China

Xiaoyu Zhao – College of Materials and Environmental Engineering, Hangzhou Dianzi University, Hangzhou 310018, PR China

Jie Liu – School of Electronics and Information Engineering, Hangzhou Dianzi University, Hangzhou 310018, PR China

Complete contact information is available at: <https://pubs.acs.org/doi/10.1021/acsnm.4c02124>

Notes

The authors declare no competing financial interest.

■ ACKNOWLEDGMENTS

The authors thank Sudan Shen for her assistance in TEM at State Key Laboratory of Chemical Engineering (Zhejiang University). T. S. Deng acknowledge financial support from Zhejiang Provincial Natural Science Foundation (Grant: LY24F050008), Zhejiang Provincial Educational Ministry Scientific Research Project (Grant: Y202352284), and National Natural Science Foundation of China (NSFC, Grant: 61905056). This work was also supported by the Fundamental Research Funds for the Provincial Universities of Zhejiang (GK239909299001-301 and GK239909299001-007) and the National Natural Science Foundation of China (Nos. 12374345).

■ REFERENCES

- (1) Giannini, V.; Fernandez-Dominguez, A. I.; Heck, S. C.; Maier, S. A. Plasmonic nanoantennas: fundamentals and their use in controlling the radiative properties of nanoemitters. *Chem. Rev.* **2011**, *111* (6), 3888–3912.
- (2) Mayer, K. M.; Hafner, J. H. Localized surface plasmon resonance sensors. *Chem. Rev.* **2011**, *111* (6), 3828–3857.
- (3) Saha, K.; Agasti, S. S.; Kim, C.; Li, X.; Rotello, V. M. Gold nanoparticles in chemical and biological sensing. *Chem. Rev.* **2012**, *112* (5), 2739–2779.
- (4) Jiang, R.; Li, B.; Fang, C.; Wang, J. Metal/Semiconductor hybrid nanostructures for plasmon-enhanced applications. *Adv. Mater.* **2014**, *26* (31), 5274–5309.
- (5) Huang, X.; Neretina, S.; El-Sayed, M. A. Gold nanorods: from synthesis and properties to biological and biomedical applications. *Adv. Mater.* **2009**, *21* (48), 4880–4910.
- (6) Atwater, H. A.; Polman, A. Plasmonics for improved photovoltaic devices. *Nat. Mater.* **2010**, *9* (3), 205–213.
- (7) Liu, M.; Guyot-Sionnest, P.; Lee, T.-W.; Gray, S. K. Optical properties of rodlike and bipyramidal gold nanoparticles from three-dimensional computations. *Phys. Rev. B* **2007**, *76* (23), 235428.
- (8) Liu, M.; Lee, T. W.; Gray, S. K.; Guyot-Sionnest, P.; Pelton, M. Excitation of dark plasmons in metal nanoparticles by a localized emitter. *Phys. Rev. Lett.* **2009**, *102* (10), 107401.
- (9) Malachosky, E. W.; Guyot-Sionnest, P. Gold Bipyramid Nanoparticle Dimers. *J. Phys. Chem. C* **2014**, *118* (12), 6405–6412.
- (10) Liu, M. Z.; Guyot-Sionnest, P. Mechanism of silver(I)-assisted growth of gold nanorods and bipyramids. *J. Phys. Chem. B* **2005**, *109* (47), 22192–22200.
- (11) Kou, X.; Zhang, S.; Tsung, C.-K.; Yeung, M. H.; Shi, Q.; Stucky, G. D.; Sun, L.; Wang, J.; Yan, C. Growth of gold nanorods and bipyramids using CTEAB surfactant. *J. Phys. Chem. B* **2006**, *110* (33), 16377–16383.
- (12) Ye, X.; Zheng, C.; Chen, J.; Gao, Y.; Murray, C. B. Using binary surfactant mixtures to simultaneously improve the dimensional tunability and monodispersity in the seeded growth of gold nanorods. *Nano Lett.* **2013**, *13* (2), 765–771.
- (13) Li, Q.; Zhuo, X.; Li, S.; Ruan, Q.; Xu, Q. H.; Wang, J. Production of Monodisperse Gold Nanobipyramids with Number Percentages Approaching 100% and Evaluation of Their Plasmonic Properties. *Adv. Opt. Mater.* **2015**, *3* (6), 801–812.
- (14) Sanchez-Iglesias, A.; Winckelmans, N.; Altantzis, T.; Bals, S.; Grzelczak, M.; Liz-Marzan, L. M. High-Yield Seeded Growth of

- Monodisperse Pentatwinned Gold Nanoparticles through Thermally Induced Seed Twinning. *J. Am. Chem. Soc.* **2017**, *139* (1), 107–110.
- (15) Chateau, D.; Desert, A.; Lerouge, F.; Landaburu, G.; Santucci, S.; Parola, S. Beyond the Concentration Limitation in the Synthesis of Nanobipyramids and Other Pentatwinned Gold Nanostructures. *ACS Appl. Mater. Interfaces* **2019**, *11* (42), 39068–39076.
- (16) Lee, J. H.; Gibson, K. J.; Chen, G.; Weizmann, Y. Bipyramid-templated synthesis of monodisperse anisotropic gold nanocrystals. *Nat. Commun.* **2015**, *6*, 7571.
- (17) Shi, Q.; Si, K. J.; Sikdar, D.; Yap, L. W.; Premaratne, M.; Cheng, W. Two-Dimensional Bipyramid Plasmonic Nanoparticle Liquid Crystalline Superstructure with Four Distinct Orientational Packing Orders. *ACS Nano* **2016**, *10* (1), 967–976.
- (18) Zhu, X.; Zhuo, X.; Li, Q.; Yang, Z.; Wang, J. Gold Nanobipyramid-Supported Silver Nanostructures with Narrow Plasmon Linewidths and Improved Chemical Stability. *Adv. Funct. Mater.* **2016**, *26* (3), 341–352.
- (19) Zhu, X.; Jia, H.; Zhu, X. M.; Cheng, S.; Zhuo, X.; Qin, F.; Yang, Z.; Wang, J. Selective Pd Deposition on Au Nanobipyramids and Pd Site-Dependent Plasmonic Photocatalytic Activity. *Adv. Funct. Mater.* **2017**, *27* (22), 1700016.
- (20) Wan, H. -Y.; Chen, J. -L.; Zhu, X.; Liu, L.; Wang, J.; Zhu, X. -M. Titania-Coated Gold Nano-Bipyramids for Blocking Autophagy Flux and Sensitizing Cancer Cells to Proteasome Inhibitor-Induced Death. *Adv. Sci.* **2018**, *5* (3), 1700585.
- (21) Fang, C.; Zhao, G.; Zhang, Z.; Ding, Q.; Yu, N.; Cui, Z.; Bi, T. AuPt Bipyramid Nanoframes as Multifunctional Platforms for In Situ Monitoring of the Reduction of Nitrobenzene and Enhanced Electrocatalytic Methanol Oxidation. *Chemistry* **2019**, *25* (30), 7351–7358.
- (22) Li, J.; Bai, Y.; Yang, B.; Zhang, J.; Chen, X.; Hayat, T.; Alsaedi, A.; Yang, Y.; Hou, J.; Tan, Z. A Multifunctional bipyramid-Au@ZnO core-shell nanoparticles as a cathode buffer layer for efficient non-fullerene inverted polymer solar cells with improved near-infrared photoresponse. *J. Mater. Chem. A* **2019**, *7* (6), 2667–2676.
- (23) Singha, T.; Medha Mishra, S.; Kumar Chini, T.; Satpati, B. Highly strained gold (Au)-palladium (Pd) core-shell nanobipyramids with extraordinary high activity and durability towards ethanol electrooxidation. *Appl. Surf. Sci.* **2022**, *604*, 154491.
- (24) Srinoi, P.; Chen, Y.-T.; Vittur, V.; Marquez, M. D.; Lee, T. R. Bimetallic Nanoparticles: Enhanced Magnetic and Optical Properties for Emerging Biological Applications. *Appl. Sci.* **2018**, *8* (7), 1106.
- (25) Huynh, K. H.; Pham, X. H.; Kim, J.; Lee, S. H.; Chang, H.; Rho, W. Y.; Jun, B. H. Synthesis, Properties, and Biological Applications of Metallic Alloy Nanoparticles. *Int. J. Mol. Sci.* **2020**, *21* (14), 5174.
- (26) Loza, K.; Heggen, M.; Eppe, M. Synthesis, Structure, Properties, and Applications of Bimetallic Nanoparticles of Noble Metals. *Adv. Funct. Mater.* **2020**, *30* (21), 1909260.
- (27) Kaur, A.; Kaur, G.; Singh, P. P.; Kaushal, S. Supported bimetallic nanoparticles as anode catalysts for direct methanol fuel cells: A review. *Int. J. Hydrog. Energy* **2021**, *46* (29), 15820–15849.
- (28) Li, J.; Zhang, W.; Ji, W. H.; Wang, J. Q.; Wang, N. X.; Wu, W. X.; Wu, Q.; Hou, X. Y.; Hu, W. B.; Li, L. Near infrared photothermal conversion materials: mechanism, preparation, and photothermal cancer therapy applications. *J. Mater. Chem. B* **2021**, *9* (38), 7909–7926.
- (29) Zhou, M.; Li, C.; Fang, J. Noble-Metal Based Random Alloy and Intermetallic Nanocrystals: Syntheses and Applications. *Chem. Rev.* **2021**, *121* (2), 736–795.
- (30) Crawley, J. W. M.; Gow, I. E.; Lawes, N.; Kowalec, I.; Kaban, L.; Catlow, C. R. A.; Logsdail, A. J.; Taylor, S. H.; Dummer, N. F.; Hutchings, G. J. Heterogeneous Trimetallic Nanoparticles as Catalysts. *Chem. Rev.* **2022**, *122* (6), 6795–6849.
- (31) Liu, L. C.; Corma, A. Bimetallic Sites for Catalysis: From Binuclear Metal Sites to Bimetallic Nanoclusters and Nanoparticles. *Chem. Rev.* **2023**, *123* (8), 4855–4933.
- (32) Linc, S.; Aslam, U.; Boerigter, C.; Morabito, M. Photochemical transformations on plasmonic metal nanoparticles. *Nat. Mater.* **2015**, *14* (6), 567–576.
- (33) Bossini, D.; Belotelov, V. I.; Zvezdin, A. K.; Kalish, A. N.; Kimel, A. V. Magnetoplasmonics and Femtosecond Optomagnetism at the Nanoscale. *ACS Photonics* **2016**, *3* (8), 1385–1400.
- (34) Kochuveedu, S. T.; Jang, Y. H.; Kim, D. H. A study on the mechanism for the interaction of light with noble metal-metal oxide semiconductor nanostructures for various photophysical applications. *Chem. Soc. Rev.* **2013**, *42* (21), 8467–8493.
- (35) Cheng, K.; Guo, Q.; Shen, Z.; Yang, W.; Wang, Y.; Sun, Z.; Wu, H. Bibliometric Analysis of Global Research on Cancer Photodynamic Therapy: Focus on Nano-Related Research. *Front. Pharmacol.* **2022**, *13*, 927219.
- (36) Xiao, Q.; Jaatinen, E.; Zhu, H. Direct photocatalysis for organic synthesis by using plasmonic-metal nanoparticles irradiated with visible light. *Chem. - Asian J.* **2014**, *9* (11), 3046–3064.
- (37) Sytwu, K.; Vadai, M.; Dionne, J. A. Bimetallic nanostructures: combining plasmonic and catalytic metals for photocatalysis. *Adv. Phys. X* **2019**, *4* (1), 1619480.
- (38) Ninakanti, R.; Dingenen, F.; Borah, R.; Peeters, H.; Verbruggen, S. W. Plasmonic Hybrid Nanostructures in Photocatalysis: Structures, Mechanisms, and Applications. *Top. Curr. Chem.* **2022**, *380* (5), 40.
- (39) Khodabandelo, F.; Shahsavarifar, S.; Nayebi, B.; Niavol, K. P.; Nayebi, B.; Varma, R. S.; Cha, J. H.; Jang, H. W.; Kim, D.; Shokouhimehr, M. Applications of nanostructured semiconductor photocatalysts for the decontamination of assorted pollutants from wastewater. *Inorg. Chem. Commun.* **2023**, *157*, 111357.
- (40) Sarina, S.; Waclawik, E. R.; Zhu, H. Photocatalysis on supported gold and silver nanoparticles under ultraviolet and visible light irradiation. *Green Chem.* **2013**, *15* (7), 1814–1833.
- (41) Zhang, X.; Chen, Y. L.; Liu, R.-S.; Tsai, D. P. Plasmonic photocatalysis. *Rep. Prog. Phys.* **2013**, *76* (4), 046401.
- (42) Ma, X. C.; Dai, Y.; Yu, L.; Huang, B. B. Energy transfer in plasmonic photocatalytic composites. *Light: sci. Appl.* **2016**, *5* (2), No. e16017.
- (43) Biffis, A.; Centomo, P.; Del Zotto, A.; Zecca, M. Pd Metal Catalysts for Cross-Couplings and Related Reactions in the 21st Century: A Critical Review. *Chem. Rev.* **2018**, *118* (4), 2249–2295.
- (44) Zhang, L.; Doyle-Davis, K.; Sun, X. Pt-Based electrocatalysts with high atom utilization efficiency: from nanostructures to single atoms. *Energy Environ. Sci.* **2019**, *12* (2), 492–517.
- (45) Cho, F.-H.; Huang, M.-H.; Chen, Y.-M.; Huang, Y.-B.; Su, C.-J.; Jeng, U. S.; Lai, Y.-H. Pt-modified dendritic gold as a highly efficient photoelectrocatalyst for the formic acid oxidation reaction. *Appl. Surf. Sci.* **2019**, *485*, 476–483.
- (46) van der Hoeven, J. E. S.; Jelic, J.; Olthof, L. A.; Totarella, G.; van Dijk-Moes, R. J. A.; Krafft, J. M.; Louis, C.; Studt, F.; van Blaaderen, A.; de Jongh, P. E. Unlocking synergy in bimetallic catalysts by core-shell design. *Nat. Mater.* **2021**, *20* (9), 1216–1220.
- (47) He, W.; Wu, X.; Liu, J.; Zhang, K.; Chu, W.; Feng, L.; Hu, X.; Zhou, W.; Xie, S. Formation of AgPt alloy nanoislands via chemical etching with tunable optical and catalytic properties. *Langmuir* **2010**, *26* (6), 4443–4448.
- (48) Xu, J.; Yun, Q.; Wang, C.; Li, M.; Cheng, S.; Ruan, Q.; Zhu, X.; Kan, C. Gold nanobipyramid-embedded silver-platinum hollow nanostructures for monitoring stepwise reduction and oxidation reactions. *Nanoscale* **2020**, *12* (46), 23663–23672.
- (49) Zhu, X.; Xu, J.; Zhang, H.; Cui, X.; Guo, Y.; Cheng, S.; Kan, C.; Wang, J. Gold nanobipyramid-embedded ultrathin metal nanoframes for in situ monitoring catalytic reactions. *Chem. Sci.* **2020**, *11* (12), 3198–3207.
- (50) Yang, X.; Wang, Q.; Qing, S.; Gao, Z.; Tong, X.; Yang, N. Modulating Electronic Structure of an Au-Nanorod-Core-PdPt-Alloy-Shell Catalyst for Efficient Alcohol Electro-Oxidation. *Adv. Energy Mater.* **2021**, *11* (26), 2100812.
- (51) Zhang, Q.; Deng, T.-S.; Dou, Y.-Q.; Wei, M.-Z.; Li, S.; Liu, J.; Cheng, Z. Trimetallic Nanostructures of Silver-Platinum Alloy Shells

on Gold Nanorods for Plasmon-Mediated Photocatalysis. *ACS Appl. Nano Mater.* **2022**, *5* (11), 17048–17058.

(52) Chen, T.; Tong, F.; Enderlein, J.; Zheng, Z. Plasmon-Driven Modulation of Reaction Pathways of Individual Pt-Modified Au Nanorods. *Nano Lett.* **2020**, *20* (5), 3326–3330.

(53) Yun, Q.; Xu, J.; Wei, T.; Ruan, Q.; Zhu, X.; Kan, C. Synthesis of Pd nanorod arrays on Au nanoframes for excellent ethanol electrooxidation. *Nanoscale* **2022**, *14* (3), 736–743.

(54) Chen, H.; Wang, F.; Li, K.; Woo, K. C.; Wang, J.; Li, Q.; Sun, L.-D.; Zhang, X.; Lin, H.-Q.; Yan, C.-H. Plasmonic Percolation: Plasmon-Manifested Dielectric-to-Metal Transition. *ACS Nano* **2012**, *6* (8), 7162–7171.

(55) Gholipour, B.; Zonouzi, A.; Shokouhimehr, M.; Rostamnia, S. Integration of plasmonic AgPd alloy nanoparticles with single-layer graphitic carbon nitride as Mott-Schottky junction toward photo-promoted H₂ evolution. *Sci. Rep.* **2022**, *12* (1), 13583.

(56) Shokouhimehr, M.; Shin, K.-Y.; Lee, J. S.; Hackett, M. J.; Jun, S. W.; Oh, M. H.; Jang, J.; Hyeon, T. Magnetically recyclable core-shell nanocatalysts for efficient heterogeneous oxidation of alcohols. *J. Mater. Chem. A* **2014**, *2* (20), 7593–7599.

(57) Alamgholiloo, H.; Rostamnia, S.; Zhang, K.; Lee, T. H.; Lee, Y.-S.; Varma, R. S.; Jang, H. W.; Shokouhimehr, M. Boosting Aerobic Oxidation of Alcohols via Synergistic Effect between TEMPO and a Composite Fe₃O₄/Cu-BDC/GO Nanocatalyst. *ACS Omega* **2020**, *5* (10), 5182–5191.

(58) Ahadi, A.; Alamgholiloo, H.; Rostamnia, S.; Liu, X.; Shokouhimehr, M.; Alonso, D. A.; Luque, R. Layer-Wise Titania Growth Within Dimeric Organic Functional Group Viologen Periodic Mesoporous Organosilica as Efficient Photocatalyst for Oxidative Formic Acid Decomposition. *ChemCatchem* **2019**, *11* (19), 4803–4809.

(59) Yong, Z.; Shi, Q.; Fu, R.; Cheng, W. Fine-Tuning Au@Pd Nanocrystals for Maximum Plasmon-Enhanced Catalysis. *Adv. Mater. Interfaces* **2021**, *8* (3), 2001686.

(60) van der Hoeven, J. E. S.; Deng, T. S.; Albrecht, W.; Olthof, L. A.; van Huis, M. A.; de Jongh, P. E.; van Blaaderen, A. Structural Control over Bimetallic Core-Shell Nanorods for Surface-Enhanced Raman Spectroscopy. *ACS Omega* **2021**, *6* (10), 7034–7046.

(61) Palik, E. D. *Handbook of Optical Constants of Solids*, Academic Press, 1985.

(62) Rakic, A. D.; Djuricic, A. B.; Elazar, J. M.; Majewski, M. L. Optical properties of metallic films for vertical-cavity optoelectronic devices. *Appl. Opt.* **1998**, *37* (22), 5271–5283.

(63) Garnett, J. C. M. XII. Colours in metal glasses and in metallic films. *Philos. Trans. R. Soc. A Math. Phys. Eng. Sci.* **1904**, *203*, 385–420.

Supporting Information

Gold Nanobipyramids Coated with Silver-Platinum Alloy Shells for Plasmonically Enhanced Photocatalytic Degradation of Methyl Orange

Er-Ji Zhang¹, Tian-Song Deng^{1,*}, Yu-Chun Cheng¹, Li-Yong Liu¹, Jia-Fei Gao¹, Jiahong
Wen¹, Xiaoyu Zhao², and Jie Liu¹

¹*School of Electronics and Information Engineering, Hangzhou Dianzi University, Hangzhou
310018, P. R. China*

²*College of Materials and Environmental Engineering, Hangzhou Dianzi University,
Hangzhou 310018, P. R. China*

* Corresponding author. E-mail: dengts@pku.edu.cn

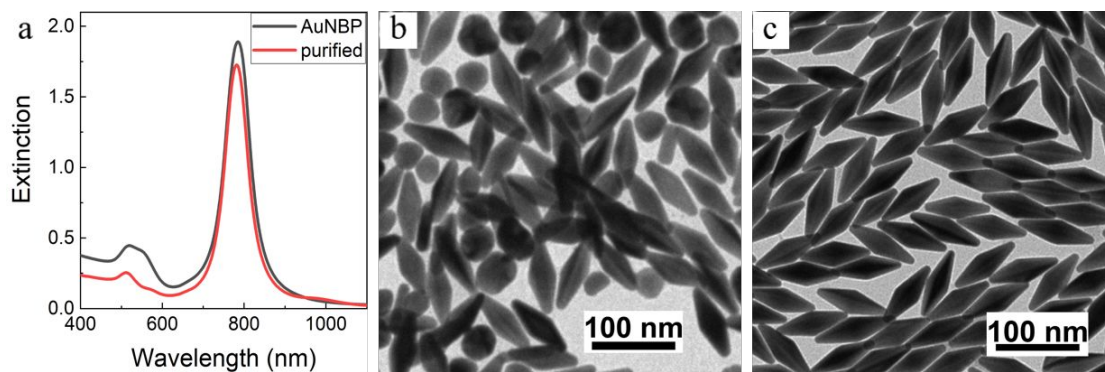


Figure S1. UV-Vis-NIR spectra and TEM images of AuNBP before and after purification. (a) UV-Vis-NIR spectra of AuNBP before (black) and after (red) purification. (b) TEM images of AuNBPs before purification. (c) TEM images of AuNBPs after purification.

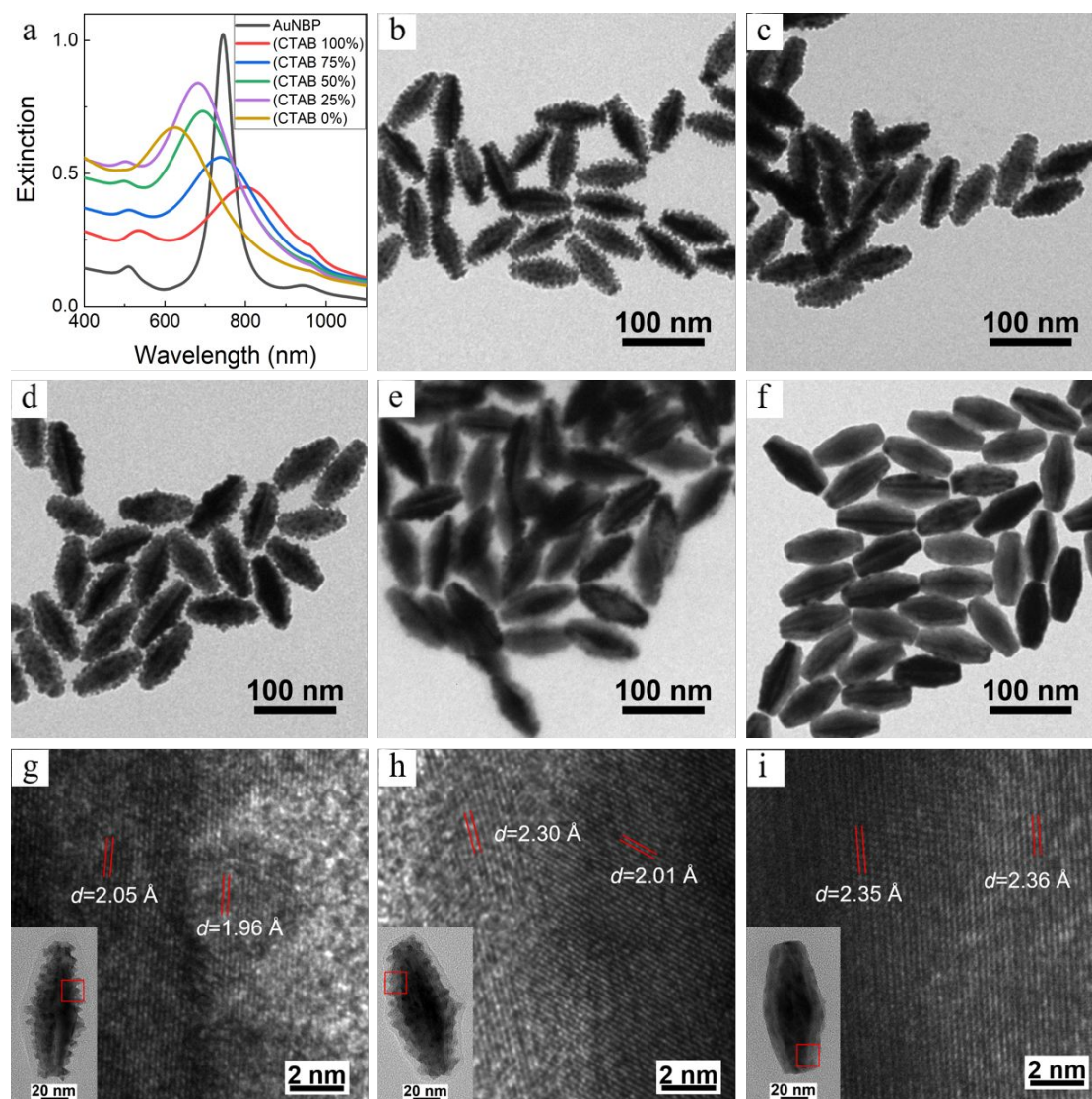


Figure S2. Morphology control of AuNBP@AgPt trimetallic structures by adjusting the type and amount of surfactant. (a) UV-Vis-NIR spectra of AuNBP@AgPt trimetallic nanoparticles synthesized under five different conditions with varying CTAB proportions (100%, 75%, 50%, 25%, and 0%). (b-f) TEM images of AuNBP@AgPt trimetallic nanoparticles synthesized under five different conditions with varying CTAB proportions (100%, 75%, 50%, 25%, and 0%). (g-i) HRTEM images of AuNBP@AgPt trimetallic nanoparticles synthesized under three different conditions with varying CTAB proportions (100%, 50%, and 0%).

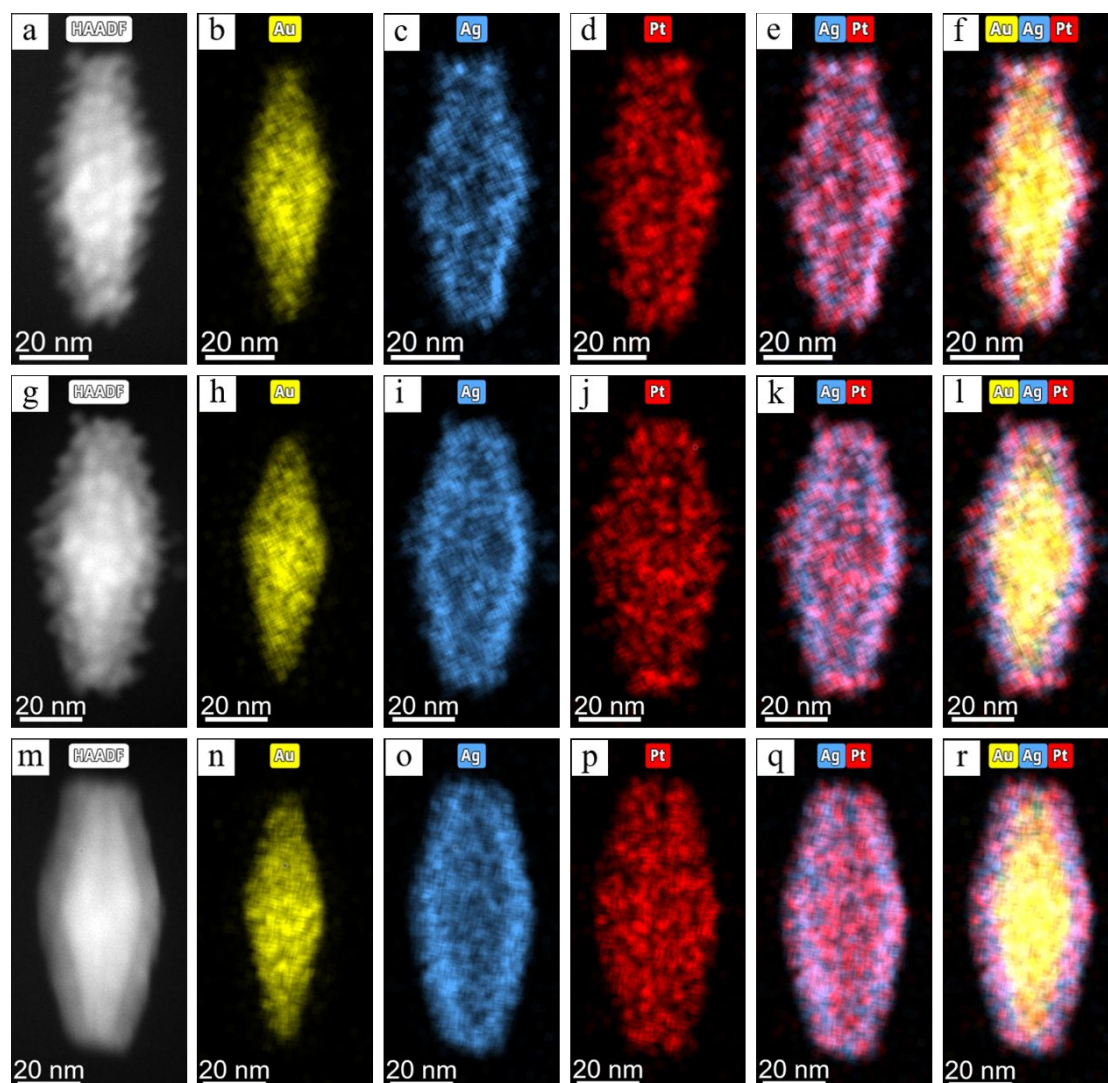


Figure S3. EDS elemental mapping images of AuNBP@AgPt trimetallic nanostructures by adjusting the type and amount of surfactants. Au, Ag, and Pt are represented in yellow, blue, and red, respectively. EDS elemental mapping images of AuNBP@AgPt nanoparticles synthesized under three different conditions with varying CTAB proportions: 100% (a-f), 50% (g-l), and 0% (m-r).

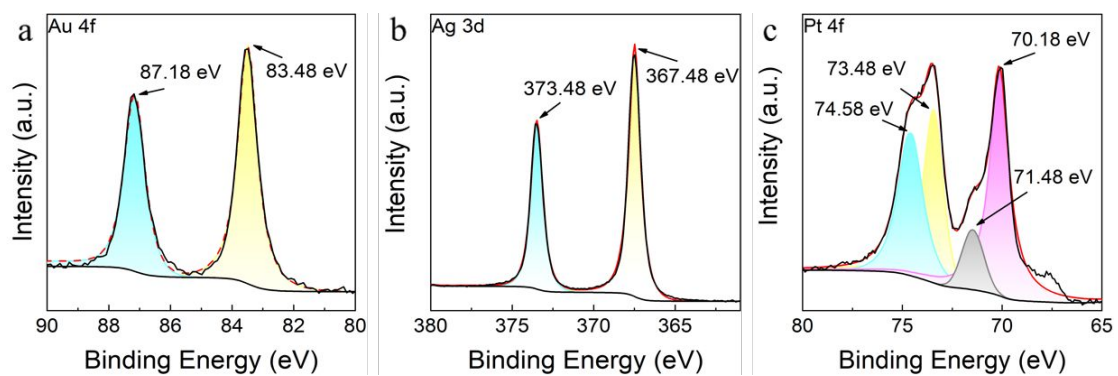


Figure S4. X-ray Photoelectron Spectroscopy (XPS) of AuNBP@AgPt Trimetallic Structure with 50% CTAB: (a) Au 4f spectrum, (b) Ag 3d spectrum, (c) Pt 4f spectrum.

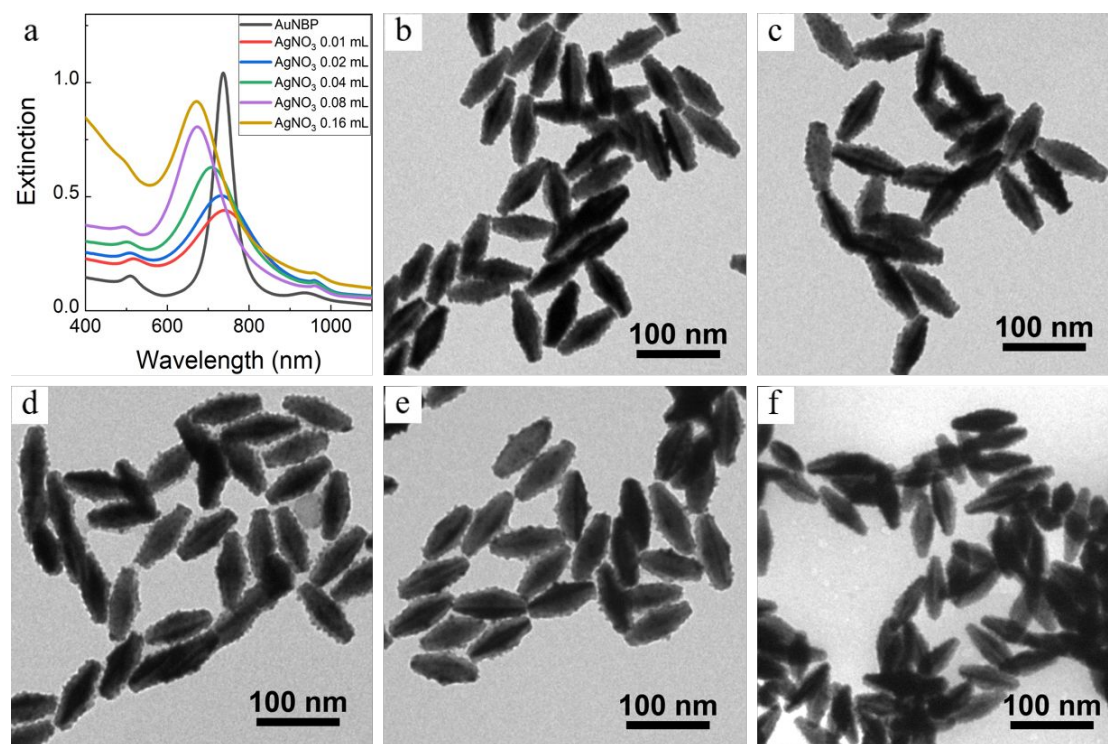


Figure S5. Morphologies of AuNBP@AgPt nanostructures with different amounts of AgNO₃. (a) UV-Vis-NIR spectra of AuNBP and AuNBP@AgPt nanostructures with different amounts of AgNO₃ (0.01 ~ 0.16 mL, 10.0 mM). (b-f) TEM images of AuNBP@AgPt nanostructures with different amounts of AgNO₃: (b) 0.01 mL, (c) 0.02 mL, (d) 0.04 mL, (e) 0.08 mL, and (f) 0.16 mL.

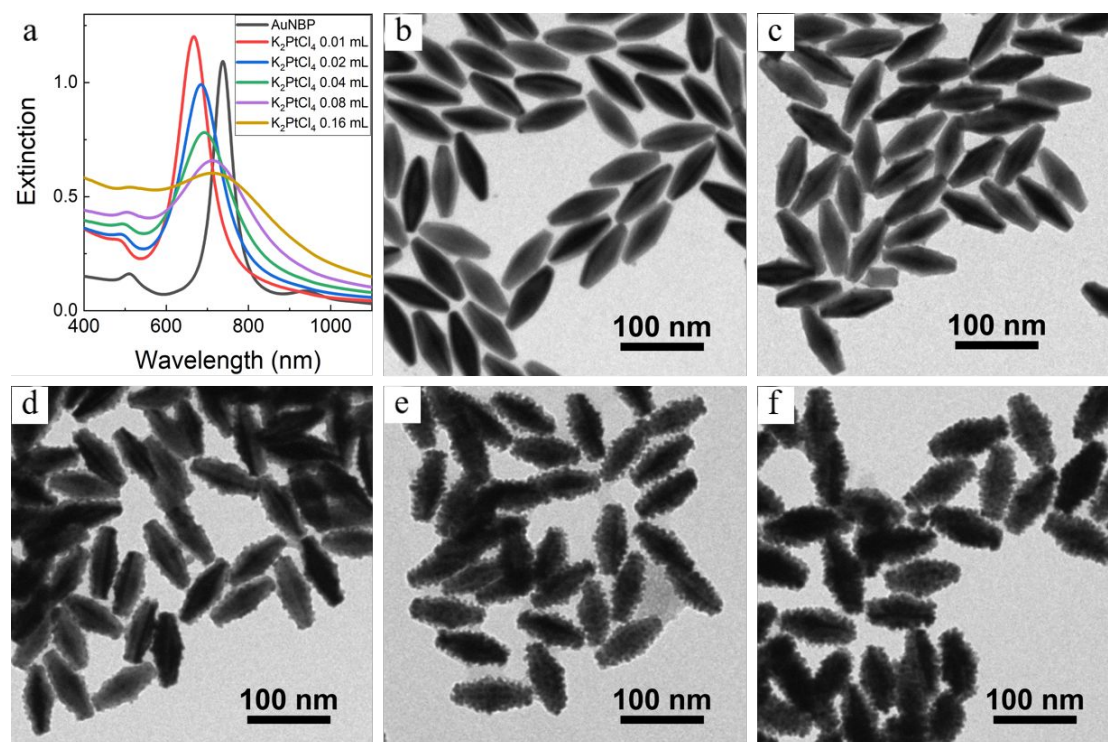


Figure S6. Morphologies of AuNBP@AgPt nanostructures with different amounts of K₂PtCl₄. (a) UV-Vis-NIR spectra of AuNBP and AuNBP@AgPt nanostructures with different amounts of K₂PtCl₄ (0.01 ~ 0.16 mL, 2.0 mM). (b-f) TEM images of AuNBP@AgPt nanostructures with different amounts of K₂PtCl₄: (b) 0.01 mL, (c) 0.02 mL, (d) 0.04 mL, (e) 0.08 mL, and (f) 0.16 mL.

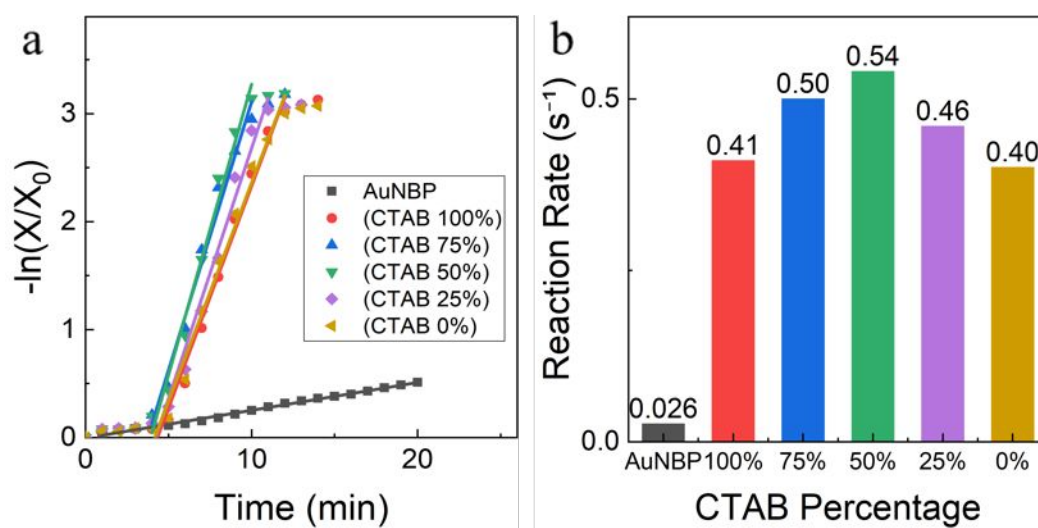


Figure S7. Plasmon-enhanced photocatalytic performance of different nanostructures of AuNBP@AgPt. (a,b) Photocatalytic performance process and rate (s^{-1} , slope) bar chart of AuNBP@AgPt nanoparticles with different surface coatings of metals.

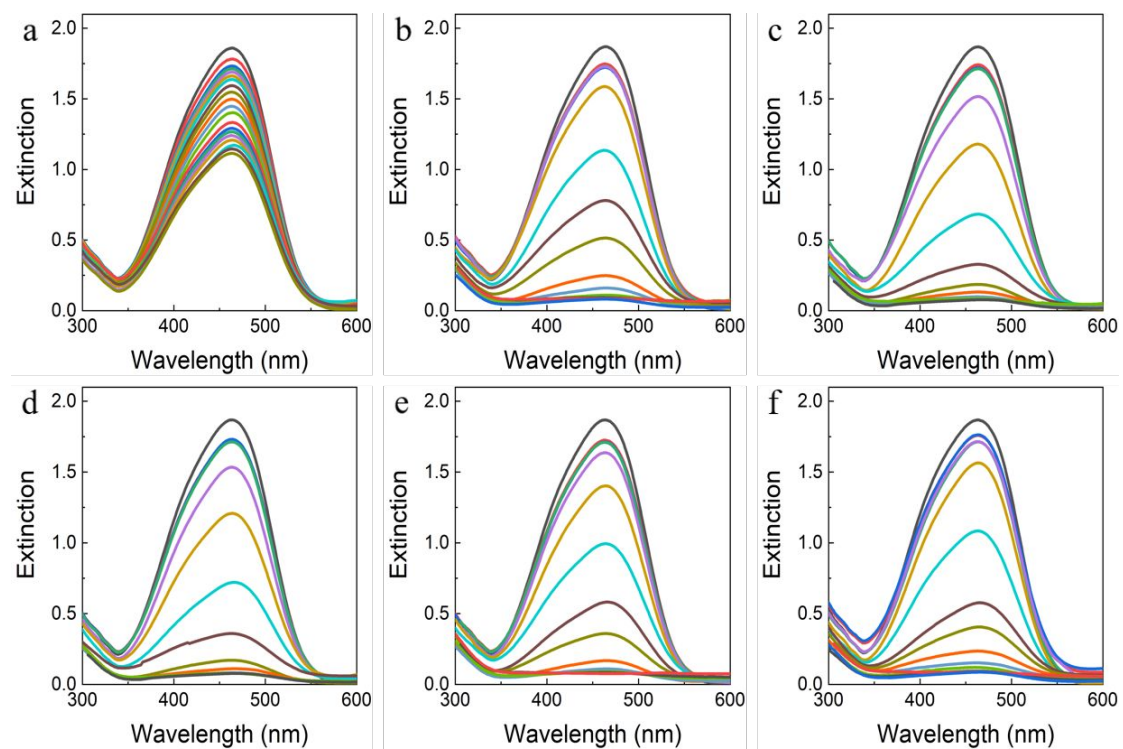


Figure S8. Raw data for the photocatalytic performances of AuNBP@AgPt nanoparticles with adjusted surfactant types and amounts. (a) Raw data for AuNBP photocatalysis. (b-f) Raw data for photocatalysis with CTAB proportions of 100% (b), 75% (c), 50% (d), 25% (e), and 0% (f).

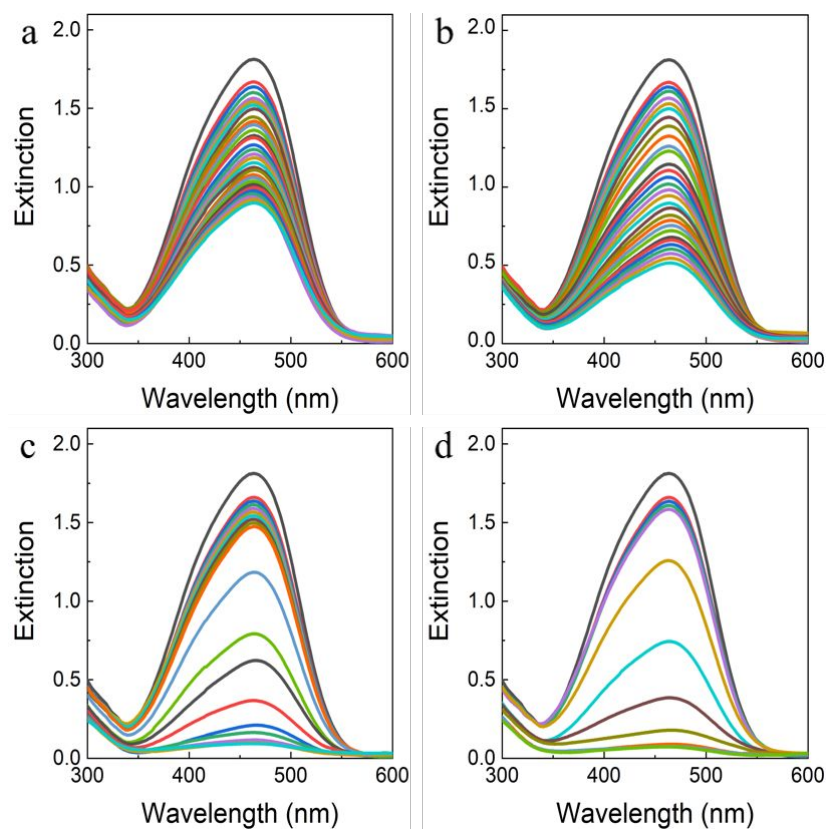


Figure S9. Raw data for the photocatalytic performances of AuNBP@AgPt nanoparticles with different metal coatings. (a) Raw data for AuNBP photocatalysis. (b) Raw data for AuNBP@Ag photocatalysis. (c) Raw data for AuNBP@Pt photocatalysis. (d) Raw data for AuNBP@AgPt photocatalysis.

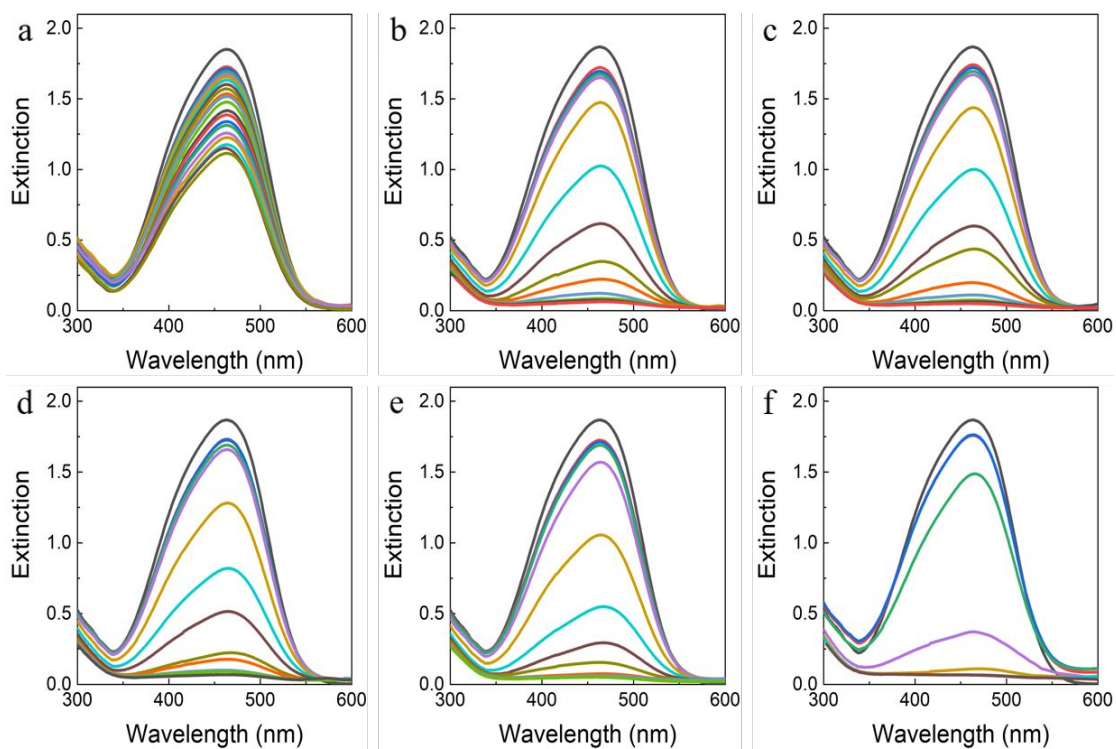


Figure S10. Raw data for the photocatalytic performances of AuNBP@AgPt nanoparticles with varying amounts of AgNO₃. (a) Raw data for AuNBP photocatalysis. (b-f) Raw data for photocatalysis with AgNO₃ amounts of (b) 0.01 mL, (c) 0.02 mL, (d) 0.04 mL, (e) 0.08 mL, and (f) 0.16 mL.

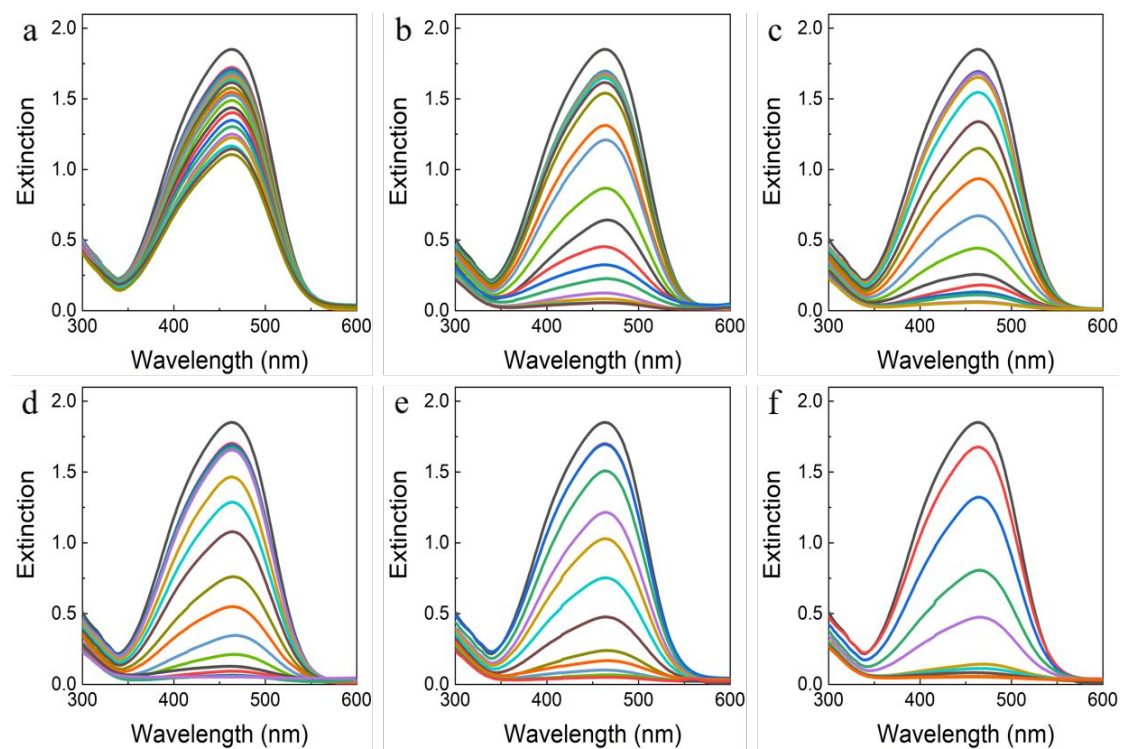


Figure S11. Raw data for the photocatalytic performances of AuNBP@AgPt nanoparticles with varying amounts of K₂PtCl₄. (a) Raw data for AuNBP photocatalysis. (b-f) Raw data for photocatalysis with K₂PtCl₄ amounts of (b) 0.01 mL, (c) 0.02 mL, (d) 0.04 mL, (e) 0.08 mL, and (f) 0.16 mL.

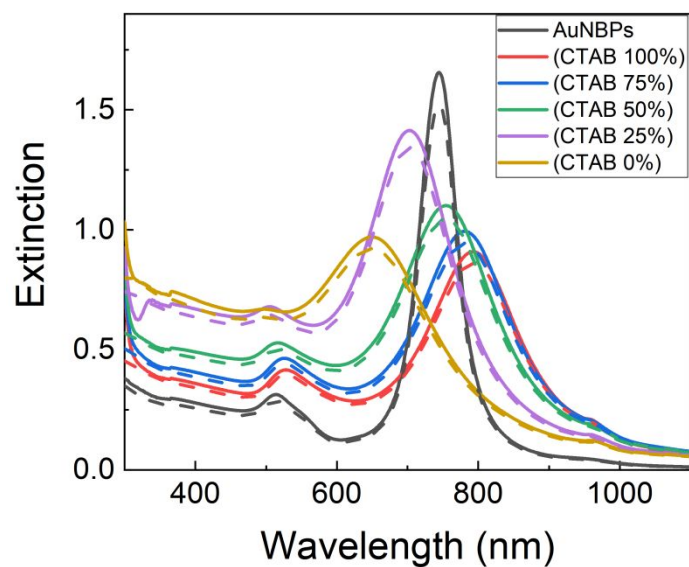


Figure S12. Comparison of the intensity of the extinction spectra before and after two rounds of washing for AuNBP and AuNBP@AgPt trimetallic structures with controlled surfactant types and ratios. Solid lines represent spectra before washing, while dashed lines represent spectra after washing.

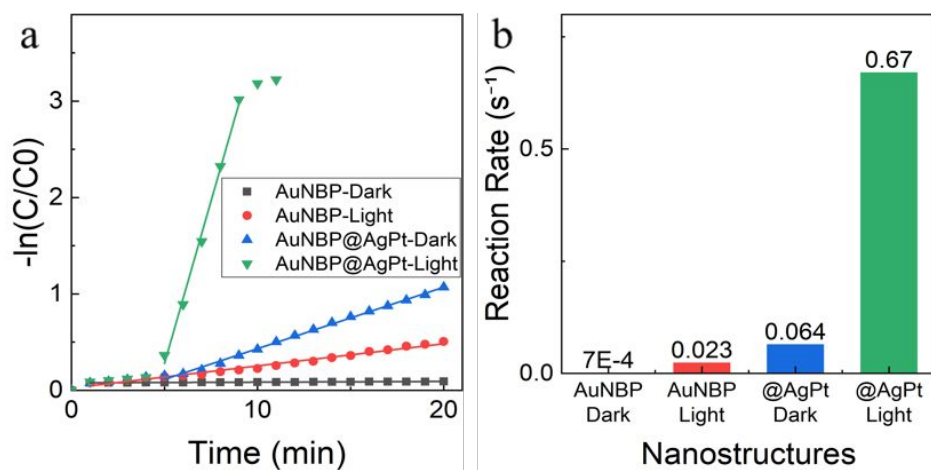


Figure S13. Comparison of the photocatalytic performance of AuNBP and AuNBP@AgPt trimetallic structures with CTAB controlled at 50%, under both illuminated and non-illuminated conditions. (a,b) Photocatalytic performance process and rate (s^{-1} , slope) bar chart of AuNBP@AgPt nanoparticles with different surface coatings of metals.

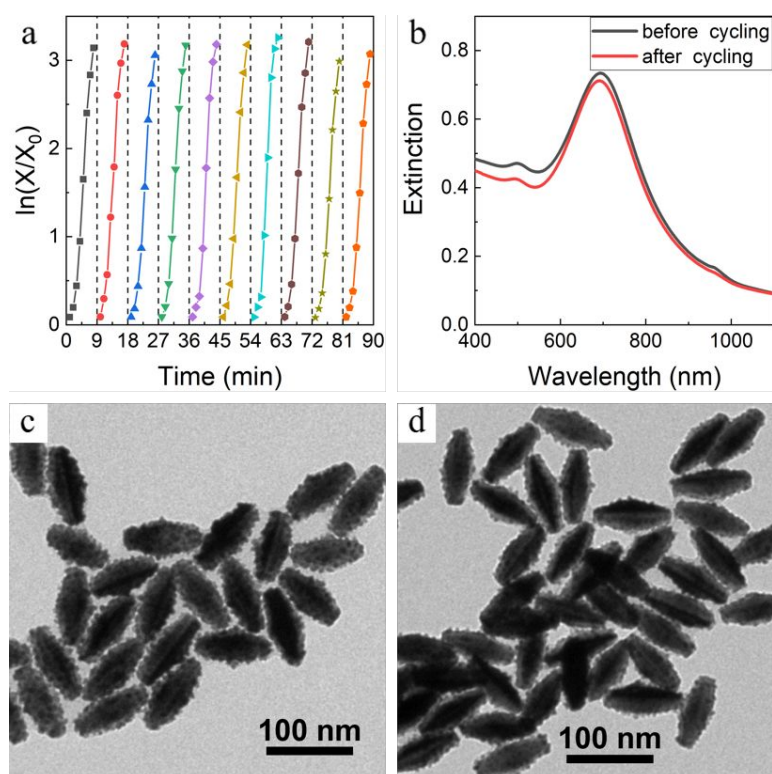


Figure S14. 10-cycle photocatalysis experiments of AuNBP@AgPt. (a) Photocatalysis process diagram for the 10-cycle photocatalysis experiment of AuNBP@AgPt. (b) Spectra before and after the 10-cycle photocatalysis experiments of AuNBP@AgPt. (c, d) TEM images of AuNBP@AgPt before (c) and after (d) the 10-cycle photocatalysis experiments.

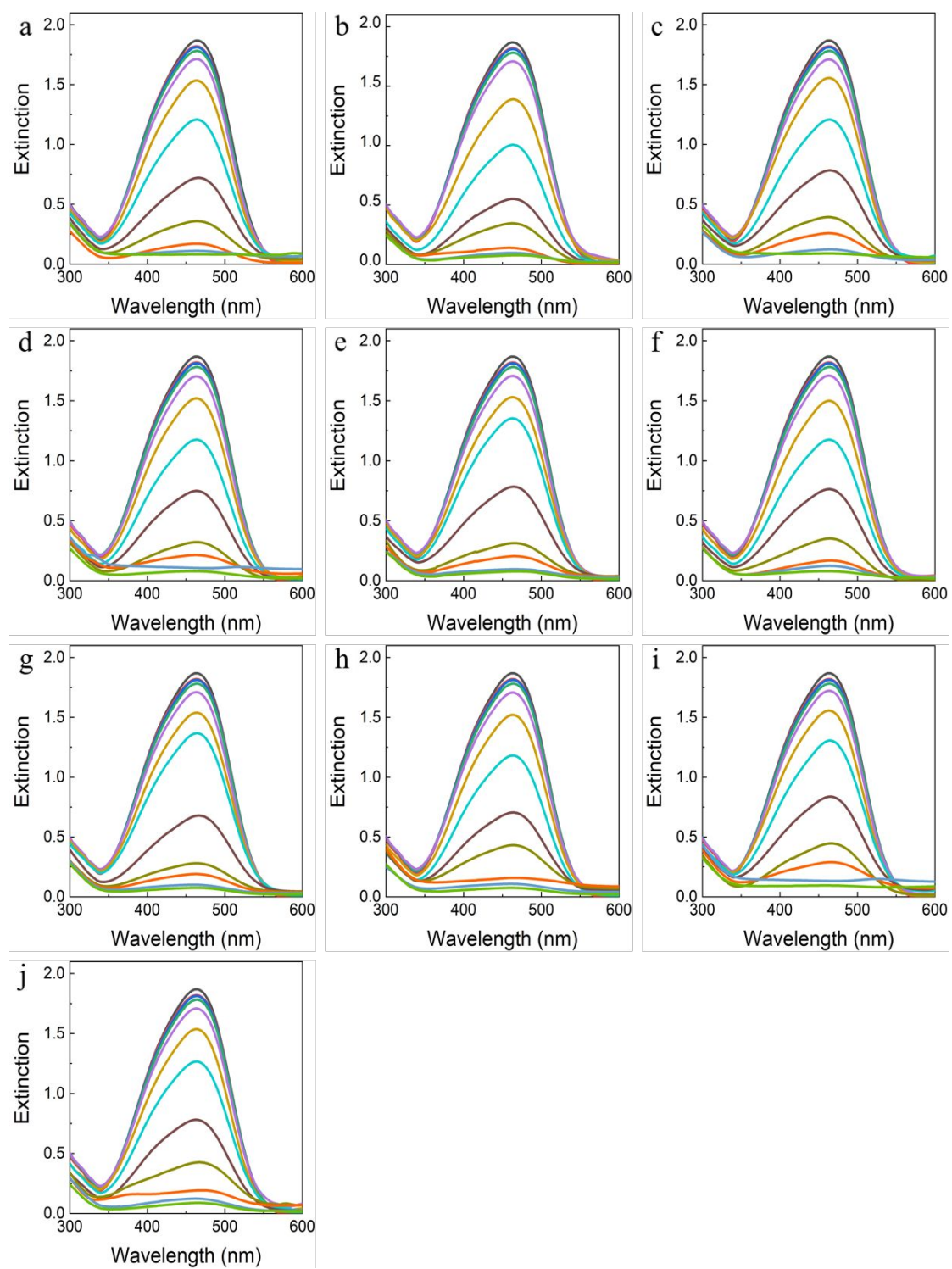


Figure S15. Raw data for the 10-cycle photocatalysis experiments of AuNBP@AgPt. (a-j) Raw data for the 1 to 10-cycle photocatalysis experiments.

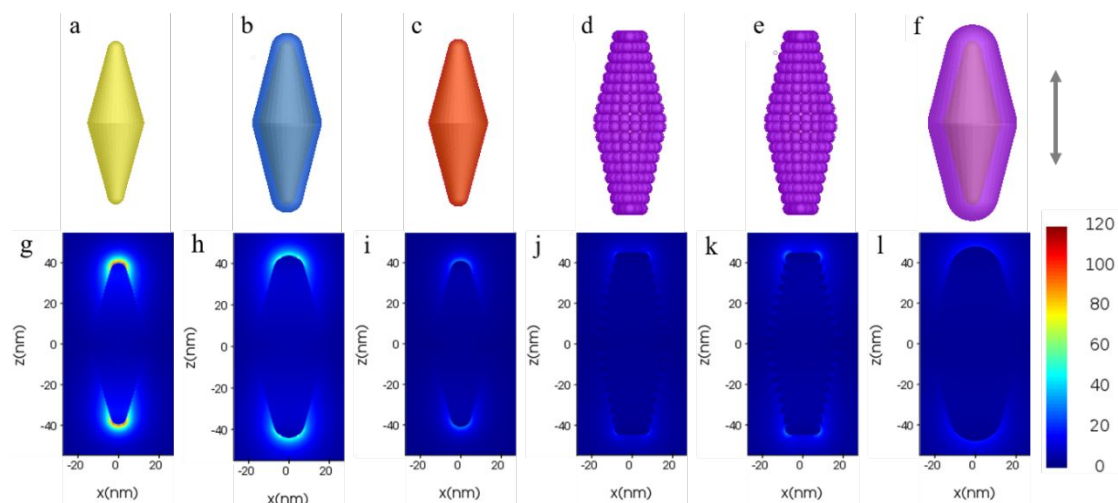


Figure S16. FDTD simulations of different nanostructures. (a-f) Modeling of various nanostructures in the FDTD simulations, from left to right: (a) AuNBP, (b) AuNBP@Ag, (c) AuNBP@Pt, (d) AuNBP@AgPt (CTAB 100%), (e) AuNBP@AgPt (CTAB 50%), (f) AuNBP@AgPt (CTAB 0%), with arrows indicating the direction of light oscillation. (g-l) Corresponding electric field distribution of a-f, with peak intensities approximately 111 (g), 85 (h), 31 (i), 23 (j), 36 (k), and 20 (l).

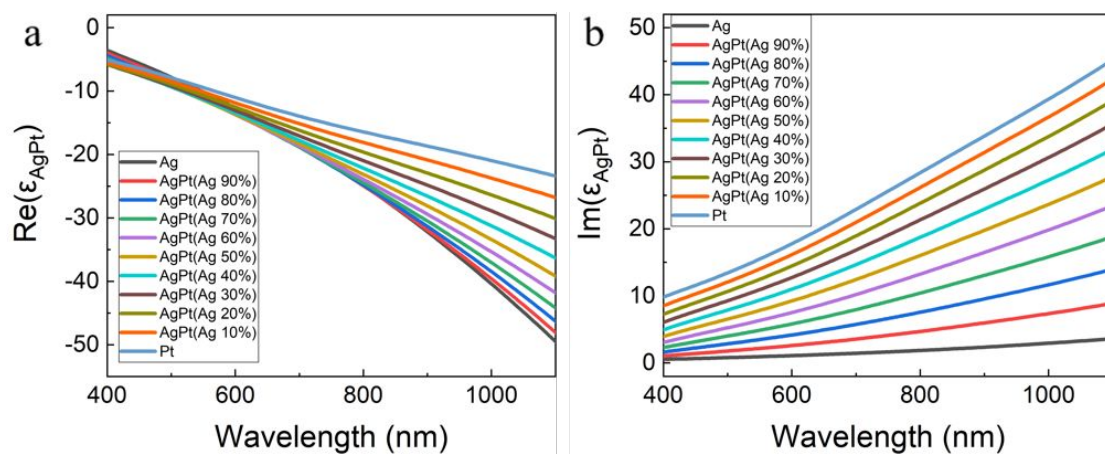


Figure S17. Dielectric function of the AgPt alloy with different Ag/Pt ratio. (a) the real part, and (b) the imaginary part.

Table S1. ICP Test Results for AuNBP@AgPt Trimetallic Structures with Varied Surfactant Types and Ratios.

Nanoparticles	Composition	Percentage content	Relative Au content
AuNBP@AgPt CTAB 100%	Au	84.65%	--
	Ag	7.44%	8.78%
	Pt	7.91%	9.35%
AuNBP@AgPt CTAB 75%	Au	80.30%	--
	Ag	12.69%	15.80%
	Pt	7.01%	8.73%
AuNBP@AgPt CTAB 50%	Au	74.60%	--
	Ag	18.53%	24.84%
	Pt	6.87%	9.21%
AuNBP@AgPt CTAB 25%	Au	60.34%	--
	Ag	33.10%	54.85%
	Pt	6.56%	10.87%
AuNBP@AgPt CTAB 0%	Au	44.14%	--
	Ag	45.39%	102.82%
	Pt	10.47%	23.71%

Table S2. The slopes (reaction rates) of the linearly fitted rate results from the photocatalytic data of the six types of nanoparticles in Figure S6a, as well as the rate multiples relative to AuNBPs.

Nanoparticles	Slope (s ⁻¹)	Relative Multiple
AuNBP	0.026	1.0
AuNBP@AgPt CTAB 100%	0.41	15.9
AuNBP@AgPt CTAB 75%	0.50	19.3
AuNBP@AgPt CTAB 50%	0.54	20.9
AuNBP@AgPt CTAB 25%	0.46	18.0
AuNBP@AgPt CTAB 0%	0.40	15.7

Table S3. The slopes (reaction rates) of the linearly fitted rate results from the photocatalytic data of the four types of nanoparticles in Figure 5b, as well as the rate multiples relative to AuNBPs.

Nanoparticles	Slope (s ⁻¹)	Relative Multiple
AuNBP	0.022	1.0
AuNBP@Ag	0.37	16.9
AuNBP@Pt	0.044	2.0
AuNBP@AgPt	0.61	27.8

Table S4. The slopes (reaction rates) of the linearly fitted rate results from the photocatalytic data of the six types of nanoparticles in Figure 5c, as well as the rate multiples relative to AuNBPs.

Nanoparticles	Slope (s ⁻¹)	Relative Multiple
AuNBP	0.024	1.0
AuNBP@AgPt AgNO ₃ 0.01mL	0.42	17.8
AuNBP@AgPt AgNO ₃ 0.02mL	0.51	21.5
AuNBP@AgPt AgNO ₃ 0.04mL	0.49	20.5
AuNBP@AgPt AgNO ₃ 0.08mL	0.62	25.8
AuNBP@AgPt AgNO ₃ 0.16mL	1.05	44.0

Table S5. The slopes (reaction rates) of the linearly fitted rate results from the photocatalytic data of the six types of nanoparticles in Figure 5d, as well as the rate multiples relative to AuNBPs.

Nanoparticles	Slope (s ⁻¹)	Relative Multiple
AuNBP	0.024	1.0
AuNBP@AgPt K ₂ PtCl ₄ 0.01mL	0.39	16.1
AuNBP@AgPt K ₂ PtCl ₄ 0.02mL	0.37	15.3
AuNBP@AgPt K ₂ PtCl ₄ 0.04mL	0.40	16.6
AuNBP@AgPt K ₂ PtCl ₄ 0.08mL	0.41	17.0
AuNBP@AgPt K ₂ PtCl ₄ 0.16mL	0.53	21.9

Table S6. The specific parameters used for synthesizing AuNBPs.

Seed Solution:

Reagents	Concentration	Volume
SC	0.01 M	5.0 mL
CTAC	0.1 M	5.0 mL
HAuCl ₄	0.01 M	0.25 mL
NaBH ₄	0.025 M	0.25 mL

Growth Solution:

Reagents	Concentration	Volume
CTAB	0.1 M	20.0 mL
HAuCl ₄	0.01 M	1.0 mL
AgNO ₃	0.01 M	0.2 mL
HCl	1.0 M	0.4 mL
AA	0.1 M	0.16 mL
Seed Solution	-	0.1 mL

Table S7. The standard procedure and reagent parameters for coating the surface of AuNBP with AgPt alloy.

Reagents	Concentration	Volume
AuNBPs (X20)	-	0.05 mL
H ₂ O	-	2.4 mL
CTAB	0.1 M	0.5 mL
CTAC	0.1 M	0.5 mL
AgNO ₃	0.01 M	0.04 mL
K ₂ PtCl ₄	0.002 M	0.04 mL
AA	0.1 M	0.04 mL

Table S8. The reagent parameters adjusted in the experiment involving the variation of surfactant ratio.

Nanoparticles	CTAB volume	CTAC volume
AuNBP@AgPt CTAB 100%	1.0 mL	0 mL
AuNBP@AgPt CTAB 75%	0.75 mL	0.25 mL
AuNBP@AgPt CTAB 50%	0.5 mL	0.5 mL
AuNBP@AgPt CTAB 25%	0.25 mL	0.75 mL
AuNBP@AgPt CTAB 0%	0 mL	1.0 mL

Table S9. The reagent parameters adjusted in the experiment involving the variation of AgNO₃ amount.

Nanoparticles	AgNO ₃ volume
AuNBP@AgPt AgNO ₃ 0.01mL	0.01mL
AuNBP@AgPt AgNO ₃ 0.02mL	0.02mL
AuNBP@AgPt AgNO ₃ 0.04mL	0.04mL
AuNBP@AgPt AgNO ₃ 0.08mL	0.08mL
AuNBP@AgPt AgNO ₃ 0.16mL	0.16mL

Table S10. The reagent parameters adjusted in the experiment involving the variation of K₂PtCl₄ amount.

Nanoparticles	K ₂ PtCl ₄ volume
AuNBP@AgPt K ₂ PtCl ₄ 0.01mL	0.01mL
AuNBP@AgPt K ₂ PtCl ₄ 0.02mL	0.02mL
AuNBP@AgPt K ₂ PtCl ₄ 0.04mL	0.04mL
AuNBP@AgPt K ₂ PtCl ₄ 0.08mL	0.08mL
AuNBP@AgPt K ₂ PtCl ₄ 0.16mL	0.16mL